Article

Immunity

Trem2 expression in microglia is required to maintain normal neuronal bioenergetics during development

Graphical abstract

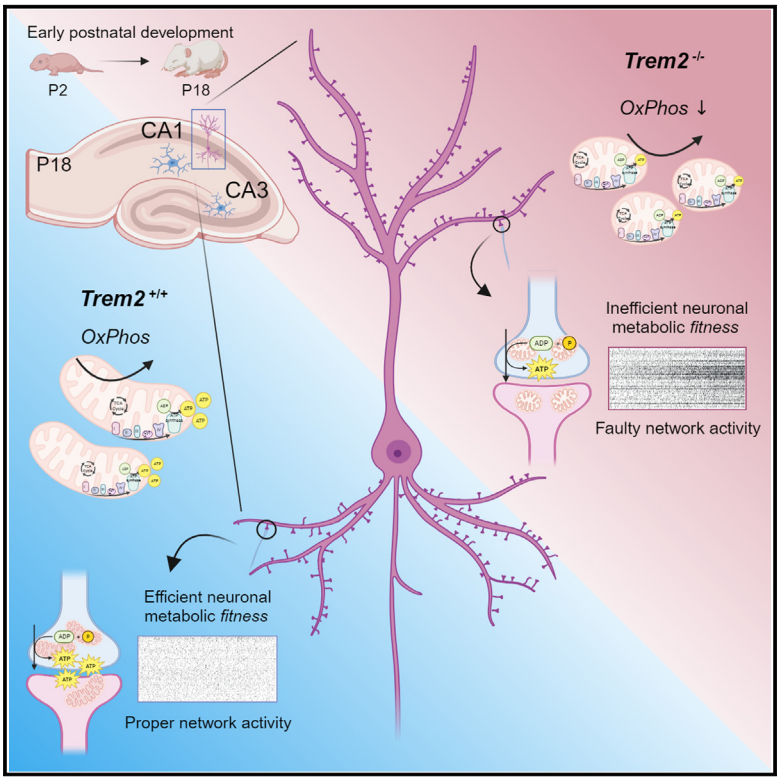

Highlights

- Lack of *Trem2* in mice impairs hippocampal neuronal bioenergetics during development
- CA1 but not CA3 neurons show reduced mitochondrial mass and metabolism
- CA1 metabolic dysfunction is later accompanied by synaptic and network alterations
- A partial reduction in Trem2 is sufficient to alter neuronal metabolic fitness

Authors

Erica Tagliatti, Genni Desiato, Sara Mancinelli, ..., Raffaella Morini, Simona Lodato, Michela Matteoli

Correspondence

michela.matteoli@hunimed.eu

In brief

Trem2 is essential for microglia-mediated synaptic refinement, but whether Trem2 contributes to shaping neuronal development remains unclear. Tagliatti, Desiato, et al. demonstrate that microglial Trem2 regulates the metabolic fitness of hippocampal neurons in a region-specific manner. Lack of Trem2-mediated communication between microglia and neurons during early development links metabolic derangements with altered synapses and circuit maturation.

Tagliatti et al., 2024, Immunity *57*, 86–105
January 9, 2024
https://doi.org/10.1016/j.immuni.2023.12.002

CellPress

CellPress
OPEN ACCESS

Immunity

Article

Trem2 expression in microglia is required to maintain normal neuronal bioenergetics during development

Erica Tagliatti,[1,2,8] Genni Desiato,[1,8] Sara Mancinelli,[3] Matteo Bizzotto,[1,3] Maria C. Gagliani,[4] Elisa Faggiani,[1] Rebeca Hernández-Soto,[1] Andrea Cugurra,[1] Paola Poliseno,[1] Matteo Miotto,[1] Rafael J. Argüello,[5] Fabia Filipello,[1,6] Katia Cortese,[4] Raffaella Morini,[1] Simona Lodato,[1,3] and Michela Matteoli[1,7,9,*]

[1]IRCCS Humanitas Research Hospital, via Manzoni 56, Rozzano, 20089 Milan, Italy
[2]Department of Clinical and Experimental Epilepsy, UCL Queen Square Institute of Neurology, University College London, London, UK
[3]Humanitas University, Department of Biomedical Sciences, Via Levi Montalcini 4, Pieve Emanuele 20072 Milan, Italy
[4]Cellular Electron Microscopy Laboratory, Department of Experimental Medicine (DIMES), Human Anatomy, Università di Genova, Via Antonio de Toni 14, 16132 Genova, Italy
[5]Aix Marseille Univ, CNRS, INSERM, CIML, Centre d'Immunologie de Marseille-Luminy, Marseille, France
[6]Department of Psychiatry, Washington University School of Medicine, St. Louis, MO, USA
[7]Institute of Neuroscience - National Research Council, 20139 Milan, Italy
[8]These authors contributed equally
[9]Lead contact
*Correspondence: michela.matteoli@hunimed.eu
https://doi.org/10.1016/j.immuni.2023.12.002

SUMMARY

Triggering receptor expressed on myeloid cells 2 (Trem2) is a myeloid cell-specific gene expressed in brain microglia, with variants that are associated with neurodegenerative diseases, including Alzheimer's disease. Trem2 is essential for microglia-mediated synaptic refinement, but whether Trem2 contributes to shaping neuronal development remains unclear. Here, we demonstrate that Trem2 plays a key role in controlling the bioenergetic profile of pyramidal neurons during development. In the absence of *Trem2*, developing neurons in the hippocampal cornus ammonis (CA)1 but not in CA3 subfield displayed compromised energetic metabolism, accompanied by reduced mitochondrial mass and abnormal organelle ultrastructure. This was paralleled by the transcriptional rearrangement of hippocampal pyramidal neurons at birth, with a pervasive alteration of metabolic, oxidative phosphorylation, and mitochondrial gene signatures, accompanied by a delay in the maturation of CA1 neurons. Our results unveil a role of Trem2 in controlling neuronal development by regulating the metabolic fitness of neurons in a region-specific manner.

INTRODUCTION

Over the last few years, the outdated concept that the brain is an immunologically privileged organ has been replaced by the observation that a continuous crosstalk occurs between the nervous system and the immune system, especially during development and aging. Microglia, the main brain residential immune cells, represent the starring actor in these processes. Besides representing a line of defense against pathogenic insults, microglia are also emerging as centrally involved in physiological functions essential for correct CNS development and plasticity, regulating neuronal apoptosis, neurogenesis, myelin formation, and removal of supernumerary synapses during development.[1–9]

Triggering receptor expressed on myeloid cells 2 (Trem2) is an immunoglobulin superfamily transmembrane receptor, expressed in the brain exclusively by microglia,[10–15] which controls the functional microglia profile by regulating their energetic metabolism.[16–20] Upon engagement with membrane-bound or soluble ligands, including lipids, lipoproteins, DNA, and bacterial products, Trem2 activates an intracellular signal transduction signaling via the adaptor proteins DAP10 and DAP12, and it enhances microglial phagocytosis of apoptotic neurons, cellular debris, bacterial products, and protein aggregates, including the neurotoxic β-amyloid peptides. Further, Trem2 promotes myeloid cell survival and proliferation[21–25] and modulates inflammatory signaling, controlling the switch from homeostatic to disease-associated microglia (DAM) state.[26] Cleavage of membrane-bound Trem2 by the α-secretases ADAM10 and ADAM17,[27,28] or translation of an alternative spliced Trem2 transcript,[29] leads to the release into the extracellular environment of soluble Trem2 (sTrem2), which maintains its biological activity.[30–32] Genome-wide association studies demonstrated that *Trem2* missense homozygous and heterozygous variants associate to neurodegenerative diseases, in particular Alzheimer disease (AD).[33–37] Specifically, *Trem2* variants deprive microglia of the dedicated sensory mechanisms required to detect damage

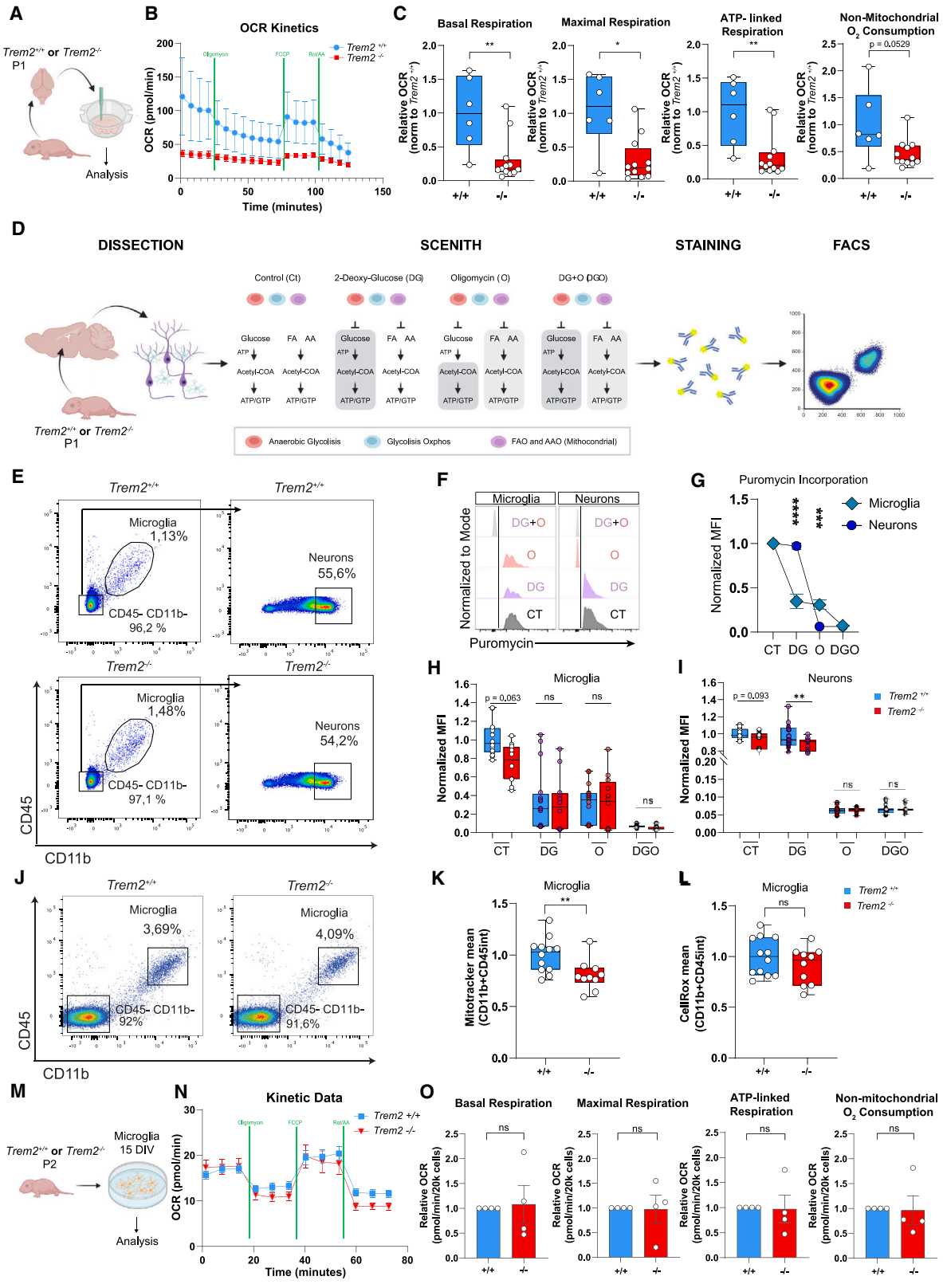

(legend on next page)

within the CNS, also preventing them from acquiring the transcriptional and functional signatures needed to fight the pathological conditions.[38,39] Accordingly, in AD models or in demyelination paradigms, lack of *Trem2* results in increased neuritic dystrophy and axonal damage around amyloid plaques.[18,40–42] The possibility that microglia, through Trem2, may shape the neuronal molecular profile and that the protein loss may force neurons to acquire altered transcriptional and molecular profiles has never been addressed.

Trem2 plays key roles also during neurodevelopment, when it controls the microglia-mediated process of supernumerary synapse elimination, influencing neuronal wiring and brain connectivity.[43–45] At these stages, the protein is highly expressed and only modestly increases as a function of age.[46,47] We focused on early developmental stages, when critical events of neuronal maturation occur, to investigate whether *Trem2* contributes to shaping the neuronal profiles. We demonstrate that lack of microglial *Trem2* functionally impacts neuronal metabolic signatures. We also demonstrate that this imbalanced pattern is associated with delayed developmental trajectory of Cornus Ammonis (CA)1 hippocampal pyramidal neurons.

RESULTS

Energetic metabolism is compromised in early post-natal neurons from *Trem2*$^{-/-}$ hippocampi

Since Trem2 regulates circulating macrophage and microglial bioenergetics,[16] we investigated the impact of *Trem2* deficiency on the overall mitochondrial metabolism in P1 acute hippocampal sections from *Trem2*$^{+/+}$ and *Trem2*$^{-/-}$ mice by measuring oxygen consumption rates (OCRs) through the Seahorse extracellular flux analyzer platform (Figure 1A). OCR measurements showed that post-natal *Trem2*$^{-/-}$ hippocampi display overall reduced mitochondrial respiration kinetics, compared with *Trem2*$^{+/+}$ (Figure 1B), with significant reduction in basal, maximal, and ATP-dependent respiration (Figure 1C), suggesting an impaired ability of *Trem2*$^{-/-}$ hippocampi to meet the overall energetic demand. Hippocampal slices from P1 *Trem2*$^{-/-}$ mice also showed a lower non-mitochondrial-related respiration (Figure 1C), indicating a lower capacity of oxidizing O_2 by other forms of enzymatic activities.[48]

We assessed whether the observed reduction was associated to microglial alterations in the absence of Trem2. Differently from P18 where the density of microglia in *Trem2*$^{-/-}$ CA1 region is lower, compared with *Trem2*$^{+/+}$,[43] no significant differences occurred in the number of hippocampal Iba1-positive cells in either CA1 or CA3 regions of P1 *Trem2*$^{-/-}$ mice (Figures S1A and S1C). Conversely, morphological analysis of P1 *Trem2*$^{-/-}$ microglia revealed a higher number of branches and junctions per cell (Figures S1B, S1D, and S1E) and a higher expression of the homeostatic receptor P2yr12 (Figure S1F). These changes were statistically significant only in the CA1 region (Figures 1D–1F, left).

To directly discriminate the contribution of different cell types to the altered metabolic phenotype, we exploited a flow cytometry-based method to functionally profile energy metabolism at single-cell resolution, namely SCENITH (single-cell energetic metabolism by profiling translation inHibition)[49] (Figure 1D). This assay relies on the concept that most of the energy deriving from glucose, amino acids, and/or lipid catabolism in living cells is consumed by protein synthesis machinery.[50] Thus, protein synthesis represents a proxy measure of global metabolic activity. We used the incorporation of puromycin combined with an anti-puro monoclonal antibody[49] as a reliable readout for measuring protein synthesis[51–53] and profiling the metabolic phenotype at single-cell resolution.

Both CD11b^{+}/CD45^{int} microglia and NeuN^{+} neurons purified from P1 hippocampi were processed (Figure 1E). We observed that *Trem2*$^{+/+}$ P1 microglia equally rely on glycolysis and mitochondria for ATP-supplying protein synthesis, since both deoxy-glucose (DG) and oligomycin (O) treatments, which block glycolysis and mitochondrial ATP synthase, respectively, decreased puromycin incorporation (Figures 1F and 1G). Conversely, P1 neurons largely rely on mitochondria as an ATP source, as they did not display any changes in puromycin incorporation after DG (Figure 1G).

By comparing *Trem2*$^{+/+}$ and *Trem2*$^{-/-}$ microglia, we observed a mild reduction in their basal metabolism (Figure 1H). The metabolic defect in *Trem2*$^{-/-}$ microglia was corroborated by mitotracker staining in CD11b^{+}/CD45^{int} microglia fluorescence-activated cell sorting (FACS)-isolated from P1 hippocampi (Figure 1J), which demonstrated a reduction of mitochondrial

Figure 1. Energetic metabolism is compromised in early post-natal neurons from Trem2$^{-/-}$ hippocampi

(A) Cartoon showing the experimental procedure.

(B) Average OCR kinetics showing the response of hippocampal slice punches from *Trem2*$^{+/+}$ and *Trem2*$^{-/-}$ newborn P1 pups to different mitochondrial inhibitors. Mean ± SEM.

(C) From left to right: basal, maximal, ATP-coupled respiration, and non-mitochondrial oxygen consumption. Box-and-whiskers plots of n = 6 vs. 12 punches from N = 3 *Trem2*$^{+/+}$ and *Trem2*$^{-/-}$ P1 newborn pups. One sample t test, **p < 0.01 and *p < 0.05.

(D) Description of the experimental design.

(E) Flow cytometry gating strategy on *Trem2*$^{+/+}$ and *Trem2*$^{-/-}$ purified CD11b^{+}CD45^{int} microglia and CD11b^{-}CD45^{-}NeuN^{+} neurons.

(F) Puromycin incorporation following the treatment with metabolic inhibitors on microglia and neurons.

(G) Puromycin mean fluorescence intensity (MFI) in *Trem2*$^{+/+}$ microglia and neurons.

(H and I) Puromycin MFI in microglia (H) and neurons (I) from *Trem2*$^{+/+}$ and *Trem2*$^{-/-}$ P1 hippocampi. Box-and-whiskers plots of N = 16 *Trem2*$^{+/+}$, N = 12 *Trem2*$^{-/-}$ P1 mice, of N = 5 independent experiments. Two-way ANOVA followed by Tukey's test, **p < 0.01.

(J) Flow cytometry gating strategy on *Trem2*$^{+/+}$ and *Trem2*$^{-/-}$ purified CD11b^{+}CD45^{int} microglia.

(K and L) FACS Mitotracker and CellROS green dye MFI from *Trem2*$^{+/+}$ and *Trem2*$^{-/-}$ P1 microglia. Box-and-whiskers plots of N = 12 *Trem2*$^{+/+}$, N = 10 *Trem2*$^{-/-}$ from P1 mice, N = 2 independent experiments. Unpaired Student's t test, **p < 0.01.

(M) Cartoon showing the experimental procedure.

(N) Left: average OCR kinetics showing the response of primary microglia from *Trem2*$^{+/+}$ or Trem2$^{-/-}$ newborn pups to different mitochondrial inhibitors.

(O) From left to right: basal, maximal, ATP-coupled respiration, and non-mitochondrial oxygen consumption. Mean ± SEM of at least n = 15 replicates from N = 4 independent *Trem2*$^{+/+}$ and *Trem2*$^{-/-}$ cultures. One sample t test.See also Figure S1.

mass (Figure 1K), without changes in reactive oxygen species (ROS) production (Figure 1L). Furthermore, primary cultured microglia isolated from P1 *Trem2*$^{-/-}$ brains and analyzed by Seahorse assay (Figure 1M) showed a negligible impairment in metabolic fitness relative to *Trem2*$^{+/+}$ (Figure 1N), without gross changes in the main OCR parameters (Figure 1O).

Unexpectedly, we observed that post-natal hippocampal neurons, whose density was unaltered in either CA1 or CA3 regions (Figures S1G and S1H), displayed a significant impairment in mitochondrial metabolism (Figure 1I), suggesting that the lack of Trem2 impacts neuronal metabolism at early developmental stages.

Single-cell sequencing of newborn hippocampi reveals a deep transcriptional rearrangements in neurons and a cell-specific engagement of metabolic processes

To investigate how the lack of *Trem2* in developing microglia impacts neuronal behavior, we transcriptionally profiled hippocampi from *Trem2*$^{+/+}$ and *Trem2*$^{-/-}$ littermates at P1, through single-cell RNA sequencing (scRNA-seq)[54] (Figures 2A and 2B). Proportionally distributed between the 2 genotypes, 26,326 cells were profiled (Figure 2C), and unsupervised clustering analysis identified 15 clusters subsequently assigned to 13 distinct cell types, according to their canonical signatures (Figures 2C and S2B).

As expected, we identified neuronal progenitors (apical progenitor [AP] and intermediate progenitor [IPC]) and glial precursors (astrocyte and oligodendrocyte precursors). Distinct classes of postmitotic excitatory neurons of the CA (CA1- and CA3-Pyr) and the dentate gyrus (granules and mossy cells) and inhibitory GABAergic interneurons derived from medial and caudal ganglionic eminences (MGE and CGE) could be distinguished. An abundant cluster of immature CA-Pyr neurons was also identified (*Ctnt2*+ cells), highlighting the dynamics of neuronal differentiation present at this stage.[55] We also found microglial cells characterized by the expression of *Trem2*, *Tmem119*, *Iba1*, *Cxc3r1*, *Csf1r*, and *Tyrobp* (Figures S2A and S2B). As previously reported, *Trem2* expression was found from early post-natal stages[46,47] to adulthood (P90, Figure S2C).

By performing differential cell abundance testing for cell types,[56] we did not observe significant changes in the composition of P1 hippocampi isolated from *Trem2*$^{+/+}$ and *Trem2*$^{-/-}$ littermates (Figures 2C, S2D, and S2E). However, differential gene expression analysis (Figure 2D) showed a significant difference in the transcriptional footprints of the excitatory pyramidal and granule cells (DG-Granule: 569 deregulated genes, 279 upregulated and 290 downregulated; CA1-Pyr: 487 deregulated genes), suggesting a prominent alteration of neuronal molecular signatures of the immature subtypes (DG-Granule and CA-Imm) and maturing CA neurons. In contrast, inhibitory neurons and non-neuronal cell types (including microglia), albeit less abundant, displayed limited transcriptional changes upon the missing Trem2 signaling (Figure 2D).

In agreement with our previously identified region-specific microglia defect in adult *Trem2*$^{-/-}$ mice,[43] we observed that CA-Imm, CA1-Pyr, and CA3-Pyr showed a distinct pattern of transcriptional deregulation with limited gene overlap (Figure 2E). These results suggest that subtype-specific responses are triggered in the absence of Trem2 signaling. Indeed, the expression of most of the genes deregulated in CA neuronal classes isolated from *Trem2*$^{-/-}$ pups was selectively altered in each class (Figure 2E), and only a small fraction was shared among the other classes (Table S1). Pathways enrichment analysis (differentially expressed genes [DEGs]) in all CA neuronal clusters revealed pervasive deregulation of key biological processes in all neuronal types (Figure 2F; Table S2) related to translational processes (eukaryotic translation initiation factor 2 [EIF2] signaling and mammalian target of rapamycin [mTOR] pathways), supporting our previous results from SCENITH analysis (Figure 1I). Further underpinning the region-specific response, genes belonging to mTOR and mitochondrial dysfunction pathways displayed a selective enrichment only in CA1-Pyr and CA-Imm neurons but not in CA3-Pyr (Figures S2G and S2H). Also, metabolic alterations were identified as a prominent feature of their neuronal footprints: major dysregulations are on the mitochondrial machinery, without transcriptional involvement of the glycolysis (Figure 2I).

The oxidative phosphorylation (OXPHOS) pathway was severely deregulated in *Trem2*$^{-/-}$ neurons. Indeed, we observed important changes in the behavior of genes associated with the respiratory chain, encoding all complexes from I to V, except complex II (Figure 2J). We found genes belonging to complex I (e.g., *Ndufa5* and *Ndufb2*), to complex III (e.g., Uqcrq), and to complex IV (e.g., *Cox6a1* and *Cox8a*), which were selectively downregulated in CA1 but not CA3 pyramidal neurons (Figure 2H). We also observed CA1 (both CA1-Pyr and CA-Imm) subtype-specific deregulation of genes belonging to complex V (e.g., *Atp5e*), coding the catalytic unit of the ATP synthase complex responsible for ATP production in the mitochondria (Figure 2H).

Overall, this evidence indicates that neurons, when microglial *Trem2* is lacking, undergo a deep transcriptional rearrangement that selectively impacts the neuronal bioenergetics. This is accompanied by a predicted inhibition of ATP synthesis in neuronal cells committed to specific regional fates (i.e., CA1 neurons).

The absence of microglial TREM2 impacts CA1 neuronal differentiation

Since mitochondrial metabolism is a key driver of cell fate transitions in the brain,[57–59] we tested whether the observed downregulation of genes involved in the OXPHOS pathways in the absence of microglial Trem2 could be involved in possible alteration of differentiation/developmental dynamics of hippocampal neuronal populations. To understand how the lack of Trem2 in microglia impacts neuronal commitment, we examined the developmental route of the neuronal lineages by inferring trajectory topology and pseudotime (Figure 3A). We first captured all the relevant cells in a standard model of hippocampus development and identified the portion of reduced dimensional space corresponding to the excitatory lineages, which included the cell types that showed the most pronounced transcriptional alteration upon lack of Trem2 in microglial cells (Figure 2D). We excluded inhibitory interneurons, as their trajectories could not be captured because the precursors are not localized within the hippocampus[60] and mossy fiber cells, whose generation occurs earlier in hippocampal neurogenesis (~E10–E12.5).[61]

Upon trajectory inference, we detected three different excitatory lineages represented by multiple cell types (Figure 3A).

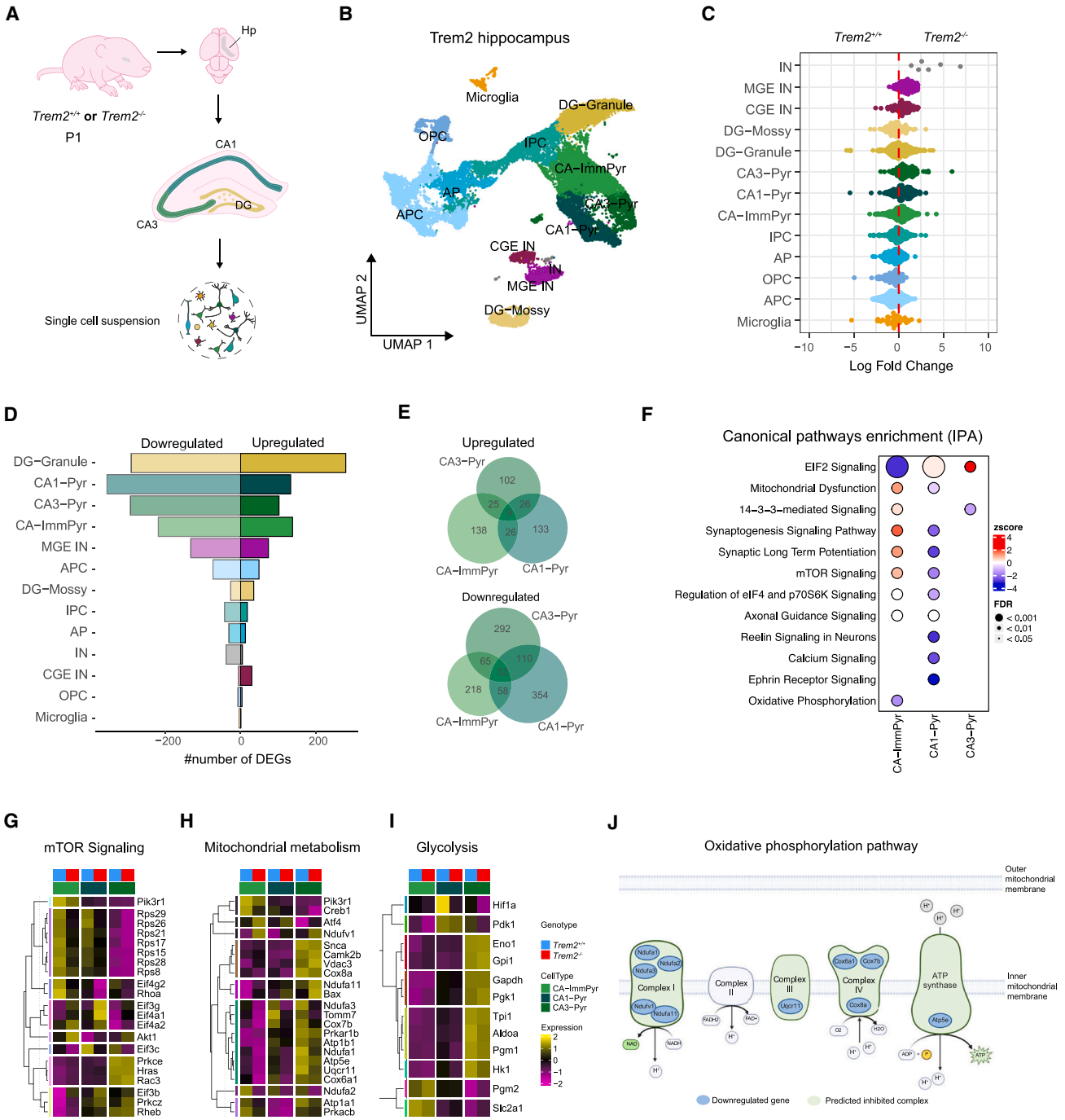

Figure 2. Single-cell transcriptomic analysis of Trem2$^{+/+}$ and Trem2$^{-/-}$ P1 hippocampal tissue reveals metabolic reprogramming of developing neurons

(A) Schematic of hippocampal dissection and dissociation from P1 *Trem2*$^{+/+}$ and Trem2$^{-/-}$ mice.

(B) Uniform manifold approximation and projection (UMAP) plot colored by cell-type annotation.

(C) Beeswarm plot of the cell abundancy changes across genotypes.

(D) Bar plot showing the number of differentially expressed genes (DEGs) for each cell type (model-based analysis of single-cell transcriptomics [MAST]-re, p adjusted < 0.05).

(E) Venn diagram showing the DEGs overlap between the selected cell types.

(F) Dot plot showing the pathway enrichment analysis for individual cell types.

(G–I) Average expression heatmap of selected cell types showing deregulated genes related to selected pathways.

(J) Schematic showing predicted inhibition complexes and downregulated genes belonging to OXPHOS pathway.

See also Figure S2.

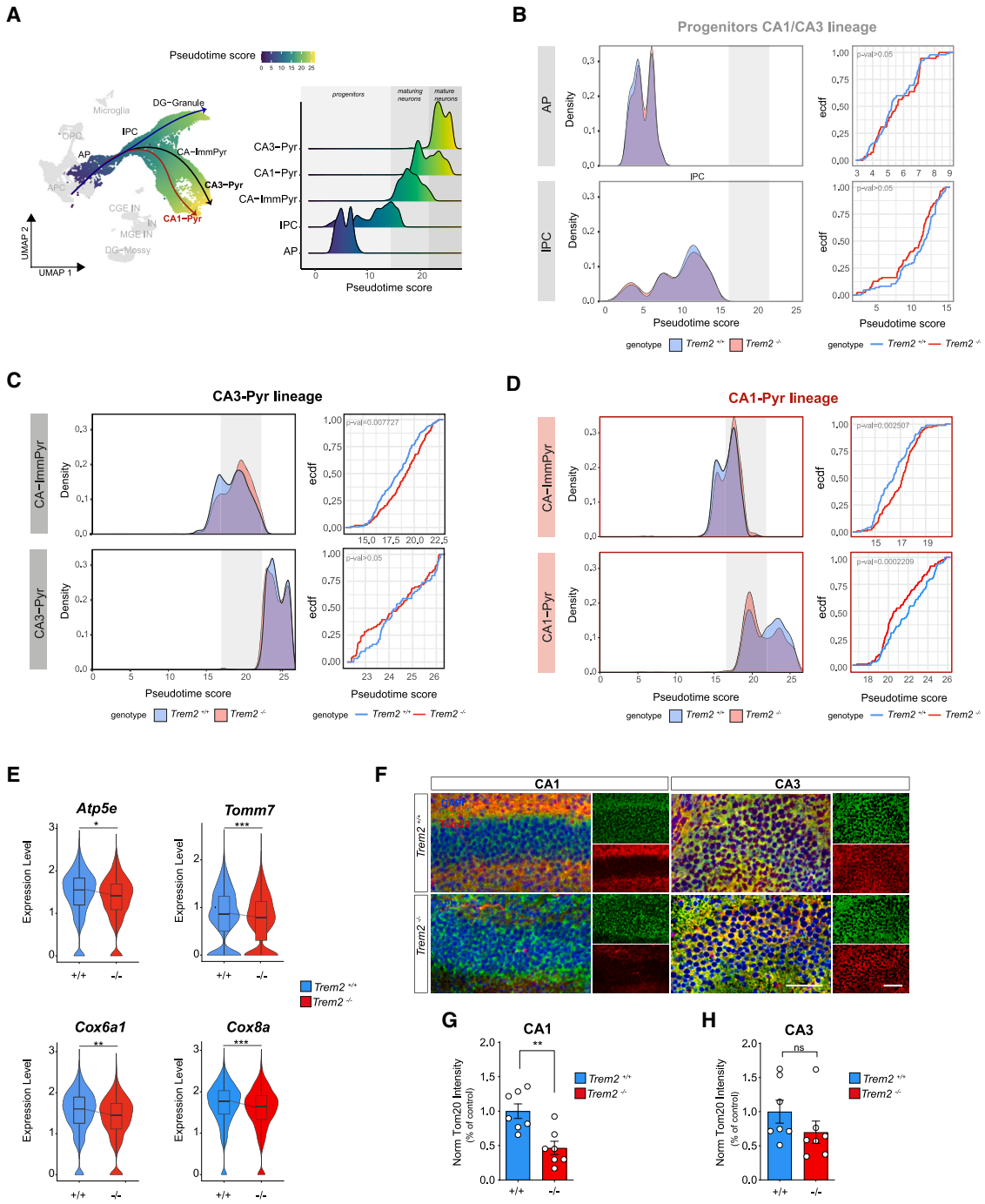

Figure 3. Mitochondrial defects in Trem2$^{-/-}$ newborn mice specifically disrupt the maturation of CA1 neurons

(A) UMAP plot showing the lineages trajectory. Density plot by cell types colored by pseudotime score value.

(B–D) Density and empirical cumulative distribution function plots show the distribution of the cells along the pseudotime between genotypes by individual cell type per lineage (KS test).

(E) Violin plots of selected DEGs associated with mitochondrial function in cells belonging to pseudotime interval = 17–22 split by genotype. MAST-re statistic test, *p adj < 0.05, **p adj < 0.01, and ***p adj < 0.001.

(F) Representative confocal images of P1 CA1 (top) and CA3 (bottom) subfields of *Trem2*$^{+/+}$ and *Trem2*$^{-/-}$ hippocampi labeled with antibodies against doublecortin (Dcx) (green) and Tom20 (red). Scale bars, 75 μm.

(G and H) Tom20 mean fluorescence intensity in CA1 and CA3 pyramidal layers, respectively. Data are presented as mean ± SEM of N = 7 *Trem2*$^{+/+}$ and *Trem2*$^{-/-}$ P1–2 pups. Data are normalized over *Trem2*$^{+/+}$ counterpart. Unpaired Student's t test, **p < 0.01.

See also Figure S3.

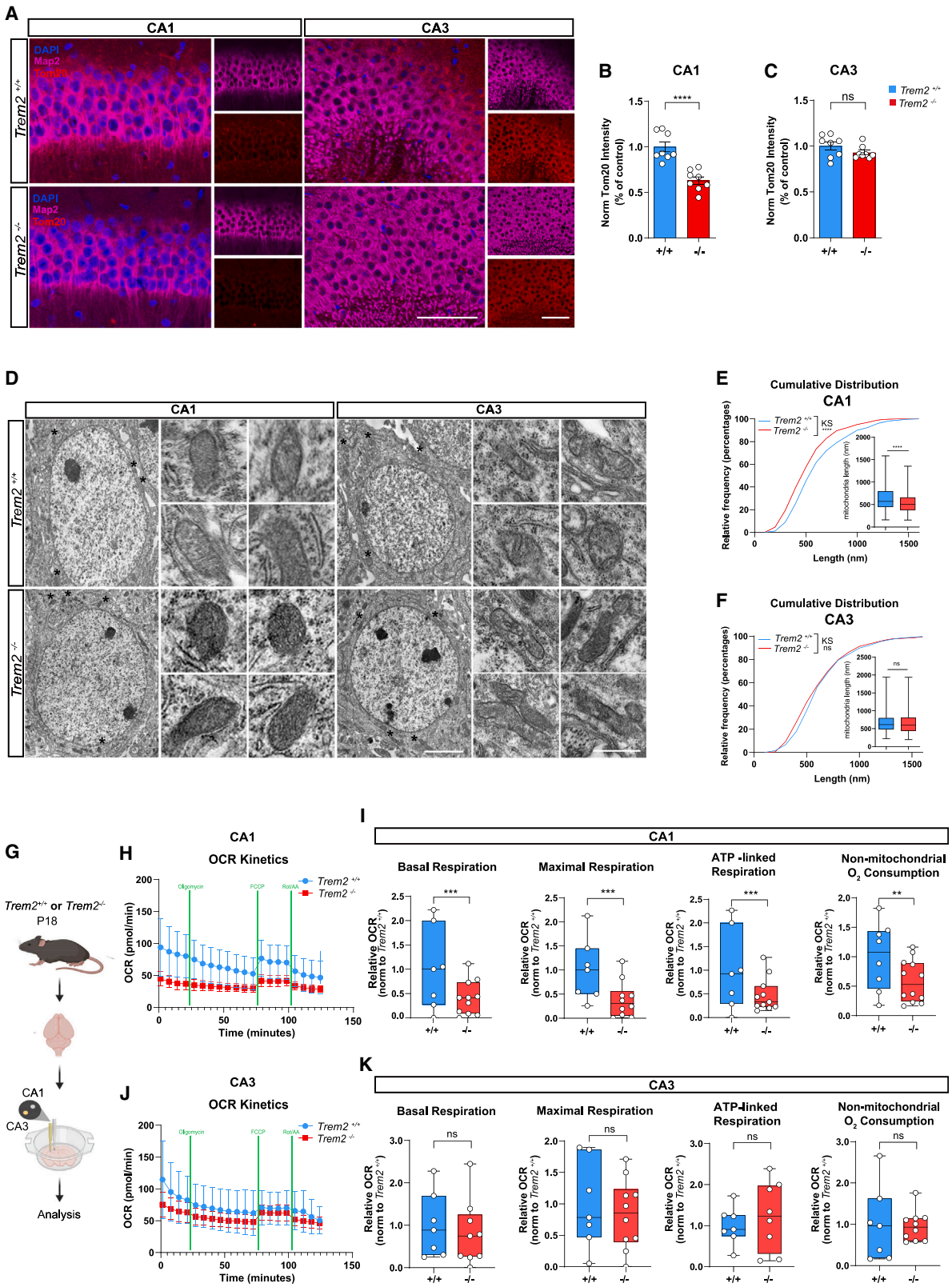

Figure 4. Mitochondrial maintenance in neurons requires Trem2 signaling

(A) Confocal images of P18 CA1 (left) and CA3 (right) subfield of *Trem2*$^{+/+}$ and *Trem2*$^{-/-}$ hippocampi labeled with antibodies (Abs) against Map2 (magenta) and Tom20 (red). Scale bars, 75 μm.

(legend continued on next page)

From the common starting point ("root") of the APs, the trajectory proceeds through IPCs to split into three distinct sublineages representing the developmental fate acquisition of the three different neuronal subtypes, which are defined by alternative ending branches (Figure 3A). No changes in the lineage topography were observed between *Trem2*$^{-/-}$ and control littermates; however, the pseudotime analysis revealed differences in the cell distribution along the trajectory branches between conditions (Figures 3B–3D). The density distribution analysis (Figures S3A and S3B) revealed a significant difference in cell frequency along the pseudotime, specifically for CA1 lineage (Kolmogorov-Smirnov [KS] test: $p = 0.02406$) and not for the other two cell lineages (KS: $p > 0.05$) (Figures S3A and S3B).

We also analyzed each lineage by parsing individual cell types for the two genotypes, focusing our attention on CA neurons. The analysis revealed that the common progenitor cells of the CA1 and CA3 lineages (AP and IPC) display similar distribution along the trajectory (Figures 3B and S3C). The analysis of the density distribution of the CA-ImmPyr exhibited a significant increase in both lineages (CA3 lineage, KS: $p = 0.007727$, Figure 3C, top panel; CA1 lineage, KS: $p = 0.02507$, Figure 3D, top panel) in the intermediate pseudotime interval (pseudotime score 17–22), which also included maturing CA1 neurons from *Trem2*$^{-/-}$, compared with *Trem2*$^{+/+}$. Of note, the accumulation of cells in the intermediate pseudotime interval coupled with a significant reduction of the terminally differentiated states (pseudotime score 22–25) only for CA1-Pyr neuronal cell types, (KS: $p = 0.0002209$, Figure 3C, bottom panel) but not for CA3-Pyr (KS: $p > 0.05$, Figure 3D, bottom panel). These data provide support for impairment in the dynamics of excitatory neuronal development in the absence of *Trem2* and highlight a delayed maturation, specifically affecting the excitatory CA1 neurons.

Next, we investigated changes in gene expression among cells exhibiting different densities across the specific pseudotime value interval (17–22, gray) and identified, among the significantly deregulated genes between conditions, key mitochondrial genes: structural regulators of the outer mitochondrial membrane, crucial for the assembly of mitochondrial complexes (e.g., *Tomm7*), showed significant downregulation in *Trem2*$^{-/-}$ cells, together with critical functional regulators of mitochondrial respiration machinery, such as *Atp5e*, *Cox6a1*, *Cox7c*, *Cox7b*, *Cox7a2*, *Cox8a*, and *Cox20* (Figure 3E; Table S1) (p adjusted < 0.05).

Finally, to assess whether the observed transcriptomic dysregulation of mitochondrial pathways in *Trem2*$^{-/-}$ hippocampal neurons was reflected by an altered mitochondrial organization, we immunostained P1 sections from *Trem2*$^{+/+}$ and *Trem2*$^{-/-}$ brains against the translocase of the outer mitochondrial membrane complex subunit 20 (Tom20, Figure 3F), a reliable marker of mitochondrial mass.[62] Confocal analysis showed a reduction in Tom20 mean intensity, significant only in CA1 region of *Trem2*$^{-/-}$ hippocampi, compared with *Trem2*$^{+/+}$ (Figures 3G and 3H).

Overall, these data indicate that lack of microglial Trem2 induces a shift in the developmental trajectory of pyramidal neurons, with a specific delay effect in the CA1 lineage, which is associated with alterations of gene programs controlling mitochondrial assembly.

Mitochondrial maintenance in neurons requires TREM2 signaling

Mitochondria are dynamic organelles that continuously remodel their morphology by fission and fusion to integrate bioenergetics and signaling in cells.[63] The reduction in Tom20 mean intensity was detected in CA1 but not CA3 region of *Trem2*$^{-/-}$ hippocampi, even at later developmental stages (P18, Figures 4A–4C). The quantitative evaluation of the mitochondrial structure in CA1 and CA3 regions of P18 *Trem2*$^{+/+}$ or *Trem2*$^{-/-}$ hippocampi by transmission electron microscopy (TEM) (Figure 4D) revealed a significant reduction in average mitochondria length in the soma of CA1 but not CA3 pyramidal neurons (Figures 4E and 4F).

In line with mitochondria ultrastructure reflecting their functionality,[64] OCR measurements in tissue punches obtained from CA1 or CA3 areas from P18 *Trem2*$^{+/+}$ and *Trem2*$^{-/-}$ mice (Figure 4G) indicated that CA1 (Figures 4H and 4I) but not CA3 (Figures 4J and 4K) subfields display a selective impairment in all OCR parameters.

These findings indicate that the genetic lack of *Trem2* in microglia induces a CA1-targeted selective impairment of OXPHOS chain accompanied by mitochondrial structural alterations, which is maintained at later developmental stages.

The CA1 hippocampal region requires high TREM2 expression for proper development

We next investigated the basis for the more prominent effect of *Trem2* deficiency in CA1 pyramidal neurons. As previously

(B and C) Quantification of Tom20 mean intensity in CA1 (B) and CA3 (C) pyramidal layer, respectively. Mean ± SEM of N = 8 *Trem2*$^{+/+}$ and *Trem2*$^{-/-}$ P18 mice. Unpaired Student's t test, ****$p < 0.0001$.

(D) Tile-scan electron micrographs of P18 CA1 (left) and CA3 (right) pyramidal somata from *Trem2*$^{+/+}$ and *Trem2*$^{-/-}$ mice. Scale bars, 3 μm. Asterisks indicate somatic mitochondria, of which zoom is shown on the right. Scale bars, 650 nm.

(E and F) Cumulative distributions and plots of somatic mitochondria length in CA1 and CA3 soma. CA1 KS test, $p < 0.0001$, CA3 KS test, $p > 0.05$. Box-and-whiskers plots of n > 300 mitochondria from N = 3 *Trem2*$^{+/+}$ and *Trem2*$^{-/-}$ P18 mice. Unpaired Student's t test, ****$p < 0.0001$.

(G) Cartoon showing the experimental procedure.

(H) Average OCR kinetics showing the response of punches of CA1 subfield from *Trem2*$^{+/+}$ and *Trem2*$^{-/-}$ P18 mice to different mitochondrial inhibitors. Mean ± SEM.

(I) From left to right: basal, maximal, ATP-coupled respiration, and non-mitochondrial oxygen consumption of CA1 brain punches. Box-and-whiskers plots of n = 8 vs. n = 12 punches from N = 3 *Trem2*$^{+/+}$ and *Trem2*$^{-/-}$ P18 mice. One sample t test, ***$p < 0.01$ and **$p < 0.01$.

(J) Average OCR kinetics showing the response of punches of CA3 subfield from *Trem2*$^{+/+}$ and *Trem2*$^{-/-}$ P18 mice to different mitochondrial inhibitors. Mean ± SEM.

(K) From left to right: basal, maximal, ATP-coupled respiration, and non-mitochondrial oxygen consumption of CA3 brain punches. Box-and-whiskers plots of n = 7 vs. 10 punches from N = 3 *Trem2*$^{+/+}$ and *Trem2*$^{-/-}$ P18 mice. One sample t test, ***$p < 0.01$, **$p < 0.01$, and *$p < 0.05$.

See also Figure S4.

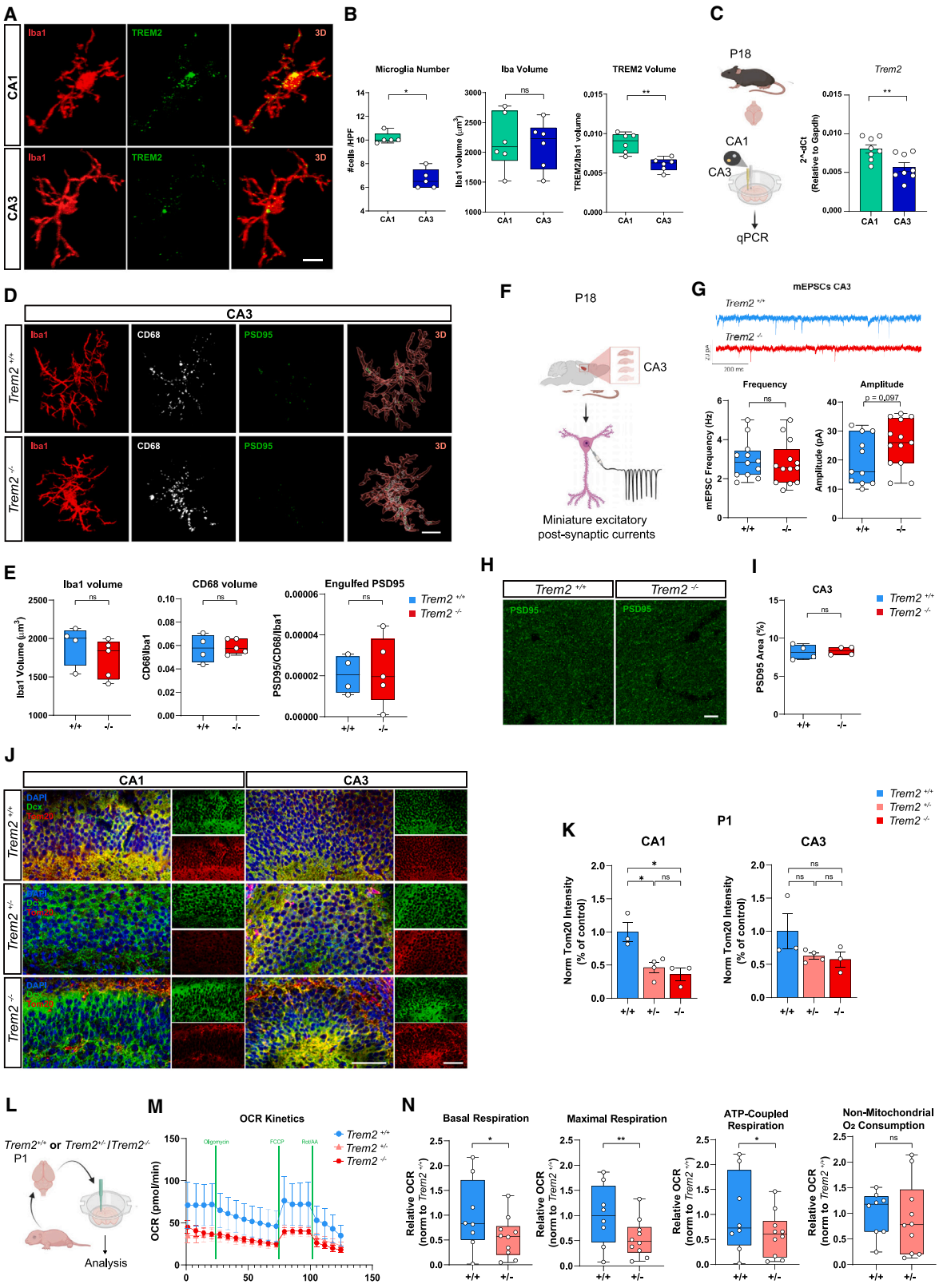

Figure 5. Trem2 is highly expressed in the CA1 region, and its partial reduction is sufficient to deregulate neuronal metabolic fitness

(A) Confocal images and 3D reconstruction of microglial cells from P18 CA1 (up) and CA3 (down) subfields of *Trem2*$^{+/+}$ hippocampi labeled with Abs against Iba1 (red) and Trem2 (green). Scale bars, 10 μm.

(legend continued on next page)

shown,[43] microglia at P18 were more enriched in the CA1 than in the CA3 region (Figures 5A and 5B, left panel), with no differences in cell volume revealed by Iba1 staining (Figures 5A and 5B, middle panel). Quantitative confocal analysis revealed that the expression of Trem2 relative to Iba1 is significantly higher in CA1 relative to CA3 (Figures 5A and 5B, right panel). Consistently, real-time quantitative PCR performed on 1-mm punches obtained from different regions of P18 hippocampal slices revealed a higher amount of *Trem2* mRNA in the CA1 region (Figure 5C). Also, while microglial phagocytosis of supernumerary synapses is impaired in the CA1 region of P18 *Trem2*$^{-/-}$ hippocampi,[43] we did not detect, in the CA3 region, any relevant difference in synapse engulfment (Figures 5D and 5E), frequency of miniature excitatory postsynaptic currents (mEPSCs, Figures 5F and 5G), and density of PSD95-labeled excitatory synapses (Figures 5H and 5I). Thus, differently from CA1, CA3 is not heavily impacted by the genetic lack of *Trem2*, suggesting that different mechanisms, independent from Trem2, may take place in this hippocampal region. Analysis of the somatosensory cortex (SSCx) revealed a significantly lower density of microglia, compared with hippocampal CA1 (Figure S5B), and a slightly lower expression of Trem2 quantified for single cell (Figure S5C, left). Quantitation of Trem2 volume in the entire fields confirmed that the protein expression was significantly higher in the CA1 region, with no difference between CA3 and SSCx (Figure S5C, right). Furthermore, similarly to the CA3 region, no differences in Tom20 expression were detected in the SSCx between *Trem2*$^{+/+}$ and *Trem2*$^{-/-}$ mice (Figure S5E). Thus, the CA1 region of the hippocampus seems to be more prominently dependent on Trem2-bearing microglia for its proper function.

To assess whether the CA1 region strictly requires microglia carrying high Trem2 expression, we exploited *Trem2*$^{+/-}$ (hemizygous) mice to test whether even partial reductions of *Trem2* expression could be sufficient for inducing neuronal metabolic derangements. We found that both P1 (Figures 5J and 5K) and P18 (Figure S5F) *Trem2*$^{+/-}$ hippocampi display reduced Tom20 mean intensity, specifically in the CA1 regions. Accordingly, OCR measurements revealed that P1 *Trem2*$^{+/-}$ hippocampi, similarly to *Trem2*$^{-/-}$ (Figures 1A–1C), display overall reduced mitochondrial respiration kinetics (Figures 5M and 5N), suggesting their impaired ability to meet the overall energetic demand.

These data indicate that neurons in the CA1 hippocampal region require high microglial Trem2 for proper differentiation and functioning and that even a partial reduction of Trem2 is sufficient to derange the neuronal metabolic fitness.

CA1 hippocampal neurons from *Trem2*$^{-/-}$ mice display synaptic alterations

We next investigated whether the metabolic alterations in *Trem2*$^{-/-}$ P18 hippocampal neurons impact synaptic function and neurotransmission. P18 mice lacking *Trem2* display a significantly higher number of excitatory synapses in the CA1 region, as contributed by the lack of supernumerary synapse elimination by *Trem2*$^{-/-}$ microglia during the period of synaptic pruning.[43] Here, we analyzed the ultrastructural features of these synapses. By TEM, we observed that *Trem2*$^{-/-}$ synapses in the CA1 pyramidal layer contain mitochondria displaying a significant reduction in length (Figures 6A and S6A). This was accompanied by reduced synaptic area and increased synaptic vesicle density (Figures 6B and S6B). No differences were, instead, observed in active zone length and docked synaptic vesicle density (Figures 6B and S6B). Differently from CA1 synapses, CA3 *Trem2*$^{-/-}$ synapses did not show alterations in mitochondria length, synaptic area, or synaptic vesicle density (Figures 6C, 6D, S6C, and S6D), also not in active zone length and docked vesicle density (Figures 6D and S6D).

To probe neuronal network functionality featuring both CA1 and CA3 regions in P18 mice lacking microglial *Trem2*, we employed multi-electrode arrays (MEAs) electrophysiology, which gives a high-throughput readout of field potential electrical activity of neuronal populations at once (Figures 6E and S6E). We measured mean firing rate (MFR) as a proxy of spontaneous

(B) Microglial number per hippocampi (left), Iba1 volume (middle), and normalized Trem2 volume on Iba1 labeling (right) per cell in CA1 and CA3 subfields. Box-and-whiskers plots of N = 6 *Trem2*$^{+/+}$ and *Trem2*$^{-/-}$ P18 mice. Unpaired Student's t test, *p < 0.05 and **p < 0.01.
(C) Left: cartoon of the experimental procedure. Right: qPCR analysis of *Trem2* mRNA in CA1 and CA3 punches from n = 8 P18 *Trem2*$^{+/+}$ mice. Unpaired Student's t test, **p < 0.01.
(D) Representative confocal image and 3D reconstruction of microglial cells from P18 CA3 subfields of *Trem2*$^{+/+}$ and *Trem2*$^{-/-}$ hippocampi labeled with Abs against PSD95 (green), CD68 (white), and Iba1 (red). Scale bars, 50 μm.
(E) Iba1 volume (left), normalized CD68 volume on Iba1 staining (middle), and PSD95 volume engulfed in microglia (right). Mean ± SEM of N = 4 *Trem2*$^{+/+}$ and N = 5 *Trem2*$^{-/-}$ P18 mice. Unpaired Student's t test.
(F) Cartoon showing the experimental procedure.
(G) Up: representative traces of mEPSC recordings in the CA3 region of hippocampal slices from P18 *Trem2*$^{+/+}$ and *Trem2*$^{-/-}$ mice. Scale bars, 20 pA, 200 ms. Down: quantification of mEPSC frequency (left) and amplitude (right) of CA3 pyramidal neurons. Box-and-whisker plots of n = 12 (*Trem2*$^{+/+}$) and 13 (*Trem2*$^{-/-}$) neurons from N = 3 *Trem2*$^{+/+}$ and *Trem2*$^{-/-}$ mice. Unpaired t test.
(H) Confocal images of CA1 (left) and CA3 (right) subfields of P18 *Trem2*$^{+/+}$ and *Trem2*$^{-/-}$ hippocampi labeled with Ab against PSD95. Scale bars, 10 μm.
(I) PSD95 volume fraction in CA1 (left) and CA3 (right) region. Mean ± SEM of N = 4 *Trem2*$^{+/+}$ and *Trem2*$^{-/-}$ P18 mice. Unpaired Student's t test.
(J) Confocal images of P1 CA1 (left) and CA3 (right) subfield of *Trem2*$^{+/+}$, *Trem2*$^{+/-}$, and *Trem2*$^{-/-}$ hippocampi labeled with Abs against Dcx (green) and Tom20 (red). Scale bars, 75 μm.
(K) Tom20 mean intensity in CA1 (left) and CA3 (right) pyramidal layers, respectively, from *Trem2*$^{+/+}$, Trem2$^{+/-}$, and *Trem2*$^{-/-}$ P1 mice. Mean ± SEM of N = 3 *Trem2*$^{+/+}$ or *Trem2*$^{-/-}$ and N = 4 *Trem2*$^{+/-}$ P1 mice. One-way ANOVA test followed by Bonferroni, *p < 0.05.
(L) Cartoon of the experimental procedure.
(M) Average OCR kinetics showing the response of hippocampal slice punches from *Trem2*$^{+/+}$ and *Trem2*$^{+/-}$ newborn P1 pups to different mitochondrial inhibitors. Mean ± SEM.
(N) From left to right: basal, maximal, ATP-coupled respiration, and non-mitochondrial oxygen consumption. Box-and-whiskers plots of n = 8 vs. n = 10 punches from N = 3 *Trem2*$^{+/+}$ and N = 4 *Trem2*$^{+/-}$ P1 newborn pups. One sample t test, **p < 0.01 and *p < 0.05.
See also Figure S5.

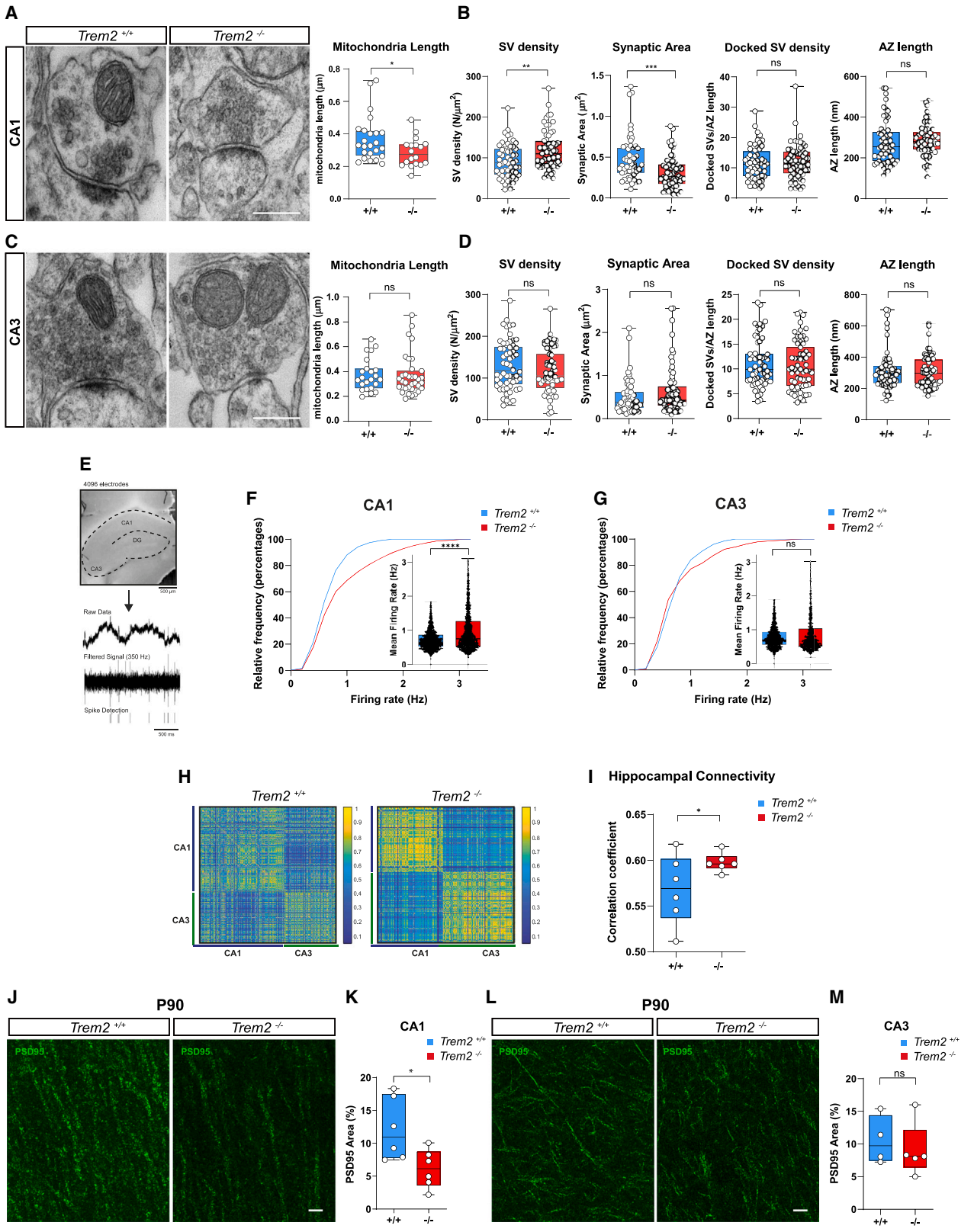

Figure 6. Trem2$^{-/-}$ hippocampal neurons display synaptic and functional alterations in a region-dependent manner

(A) Electron micrograph of synapses in the CA1 pyramidal layer of P18 *Trem2*$^{+/+}$ and *Trem2*$^{-/-}$ mice. Scale bars, 200 nm. Box-and-whiskers plot of synaptic mitochondria length of n = 24 (*Trem2*$^{+/+}$) or 18 (*Trem2*$^{-/-}$) synapses from N = 3 *Trem2*$^{+/+}$ and *Trem2*$^{-/-}$ P18 mice. Mann-Whitney U test, *p < 0.05.

(legend continued on next page)

neuronal activity in whole hippocampal slices (Figure 6E) and found that MFR in CA1 (Figure 6F) but not in CA3 (Figure 6G) was significantly higher in *Trem2*$^{-/-}$ P18 slices. Such an effect was mainly due to an average increase in neuronal spontaneous activity and not in the number of firing cells[65] (Figure S6F). Also, P18 *Trem2*$^{-/-}$ hippocampi showed a higher synchronicity and connectivity, compared with Trem2$^{+/+}$ ones (Figures 6H and 6I). The increase in spontaneous neuronal activity is in line with the higher density of excitatory synaptic markers and miniatures events that we already demonstrated in P18 *Trem2*$^{-/-}$ mice.[43]

We have previously shown that at more mature developmental stages (P90), the hippocampal amount of PSD95 protein in *Trem2*$^{-/-}$ hippocampus undergoes a reduction, compared with P18, in the absence of changes in spine density.[43] By specifically analyzing different hippocampal regions, we now demonstrate that the synaptic impoverishment at P90 occurs specifically in the CA1 but not the CA3 region of *Trem2*$^{-/-}$ mice (Figures 6J–6M). These data suggest that the metabolic faultiness in the *Trem2*$^{-/-}$ CA1 region may cause defective synapse strengthening in the adult (P90).

Neurons from *Trem2*$^{-/-}$ mice display mitochondrial defects and faulty differentiation even after their isolation from the brain context

We next wondered whether the metabolic derangement detected in neurons from *Trem2*$^{-/-}$ brains required the continuous proximity of microglial cells or relied on cell-autonomous mechanisms. To address this question, primary neurons were harvested from P1 hippocampi of *Trem2*$^{+/+}$ and *Trem2*$^{-/-}$ mice, maintained in culture for 4 days (4 days *in vitro* [DIV]) and then assayed for OCR measurements (Figure 7A). Results showed that the mitochondrial fitness of *Trem2*$^{-/-}$ neurons is significantly altered (Figure 7B). Indeed, 4 DIV Trem2$^{-/-}$ neurons showed an impairment to meet their energetic demand (Figure 7C). Non-mitochondrial respiration was also defective in *Trem2*$^{-/-}$ neurons (Figure 7C). By virtue of the transcriptional signature emerging from scRNA-seq, involving most of genes linked to OXPHOS and mitochondrial dysfunction pathways, these data indicate that the functional defects in metabolic fitness have been transcriptionally imprinted during earlier developmental times and that this signature intimately predetermines the mitochondrial functional outcome. To parallel the neuronal metabolic derangement observed with extracellular flux measurements in 4 DIV cultures, a significant reduction of Tom20 (Figure 7D) was detected in both the soma and neurites of *Trem2*$^{-/-}$ neurons, compared with *Trem2*$^{+/+}$ (Figures 7E and 7F). Furthermore, a reduction in mitochondrial ATP production at the neuronal soma was detected by live-imaging experiments (Figure 7G). Also, Sholl analysis (Figure 7H) provided evidence of an overall reduction in neuronal ramification (Figure 7I) and in primary neurite length (Figure 7J), supporting the hypothesis of a developmentally delayed neuronal maturation.

Given that the composition of Na^+ and K^+ channels significantly changes along with the maturation of neuronal cells,[66] an electrophysiological characterization of 4 DIV neurons was performed. We recorded current-voltage (I-V) relationships to estimate inward Na^+ and outward K^+ currents (Figure 7K). The I-V curve demonstrated a significant reduction in Na^+ but not in K^+ current density in *Trem2*$^{-/-}$ neurons, compared with *Trem2*$^{+/+}$ neurons (Figures 7L and 7M). Moreover, *Trem2*$^{-/-}$ neurons displayed a more depolarized resting membrane potential (E_m) than Trem2$^{+/+}$ neurons (Figure 7N), which is generally considered a feature of neuronal immaturity.[67,68] Finally, Trem2$^{-/-}$ neurons showed slightly higher electrical resistivity (R_m) and lower capacitance (C_m) values than Trem2$^{+/+}$ (Figure 7O). These data indicate that even in primary culture, neurons from Trem2$^{-/-}$ hippocampi display defective metabolic properties and a delay in maturation, paralleling what was observed in the *in vivo* setting (Figures 1A–1C, 3A–3D, and 3F–3H).

We next asked whether the excitatory neurotransmission derangement that was observed *in vivo* at P18 (Figures 6E–6I) was also detectable in mature cultures of neurons from *Trem2*$^{-/-}$ hippocampi. We have previously shown that the electrophysiological properties of 14 DIV neurons from *Trem2*$^{-/-}$ or *Trem2*$^{+/+}$ mice are not different.[43] Also, neuronal resting potential and passive properties (resistivity; capacitance) were similar among the two populations, in both CA1 and CA3 subfields of P18 slices (Figures S6G and S6H) and 14 DIV cultured neurons (Figures S7D and S7E). However, and similarly to the *ex vivo* setting, mitochondria remained defective in neuronal somata and synaptic contacts of 14 DIV neurons from *Trem2*$^{-/-}$ mice

(B) Synaptic vesicle (SV) density, synaptic area, docked SVs density, and active zone length in CA1 pyramidal layer synapses of P18 *Trem2*$^{+/+}$ and *Trem2*$^{-/-}$ mice. Box-and-whiskers plots of n = 56 (*Trem2*$^{+/+}$) or 59 (*Trem2*$^{-/-}$) synapses from N = 3 *Trem2*$^{+/+}$ and *Trem2*$^{-/-}$ mice. Mann-Whitney U test, **p < 0.01 and ***p < 0.001.
(C) Left: electron micrographs of synapses in the CA3 pyramidal layer of P18 *Trem2*$^{+/+}$ and *Trem2*$^{-/-}$ mice. Scale bars, 200 nm. Right: box-and-whiskers plots of synaptic mitochondria length of n = 23 (*Trem2*$^{+/+}$) or 35 (*Trem2*$^{-/-}$) synapses from N = 3 *Trem2*$^{+/+}$ and *Trem2*$^{-/-}$ P18 mice. Mann-Whitney U test.
(D) SV density, synaptic area, docked SVs density, and active zone length in CA3 pyramidal layer synapses of *Trem2*$^{+/+}$ and *Trem2*$^{-/-}$ mice. Box-and-whiskers plots of n = 58 (*Trem2*$^{+/+}$) or 63 (*Trem2*$^{-/-}$) synapses from N = 3 *Trem2*$^{+/+}$ and *Trem2*$^{-/-}$ mice. Mann-Whitney U test.
(E) Up: image of a coronal hippocampal slice from a P18 *Trem2*$^{-/-}$ mouse on the CMOS multi-electrode array. Scale bars, 500 μm. Down: raw data, filtered signal (350 Hz), and spike detection originating from an electrode.
(F and G) Cumulative frequency distributions and quantification of average spontaneous firing rates from neurons in CA1 (F) and CA3 (G) subfields of *Trem2*$^{+/+}$ and *Trem2*$^{-/-}$ P18 mice. Box-and-whiskers plots of n > 600 neurons from N = 6 hippocampal slices from 3 mice. Dots represents individual firing units. Unpaired Student's t test, ****p < 0.0001.
(H) Cross-correlation matrix of neuron pairs during CA1 and CA3 spontaneous activity in *Trem2*$^{+/+}$ and *Trem2*$^{-/-}$ P18 male mice.
(I) Average correlation coefficient from all active neuron pairs in CA1 and CA3 regions in *Trem2*$^{+/+}$ and *Trem2*$^{-/-}$ mice. Box-and-whiskers plots of n = 6 slices from N = 3 P18 *Trem2*$^{+/+}$ and *Trem2*$^{-/-}$ mice. One-sided unpaired Student's t test, * p < 0.05.
(J and K) Confocal images of CA1 (J) and CA3 (K) subfields of P90 *Trem2*$^{+/+}$ and *Trem2*$^{-/-}$ hippocampi labeled with Ab against PSD95. Scale bars, 10 μm.
(L and M) PSD95 volume fraction in CA1 (L) and CA3 (M) regions. Box-and-whiskers plots of N = 6 *Trem2*$^{+/+}$ and N = 6 *Trem2*$^{-/-}$ P90 mice. Unpaired Student's t test.
See also Figure S6.

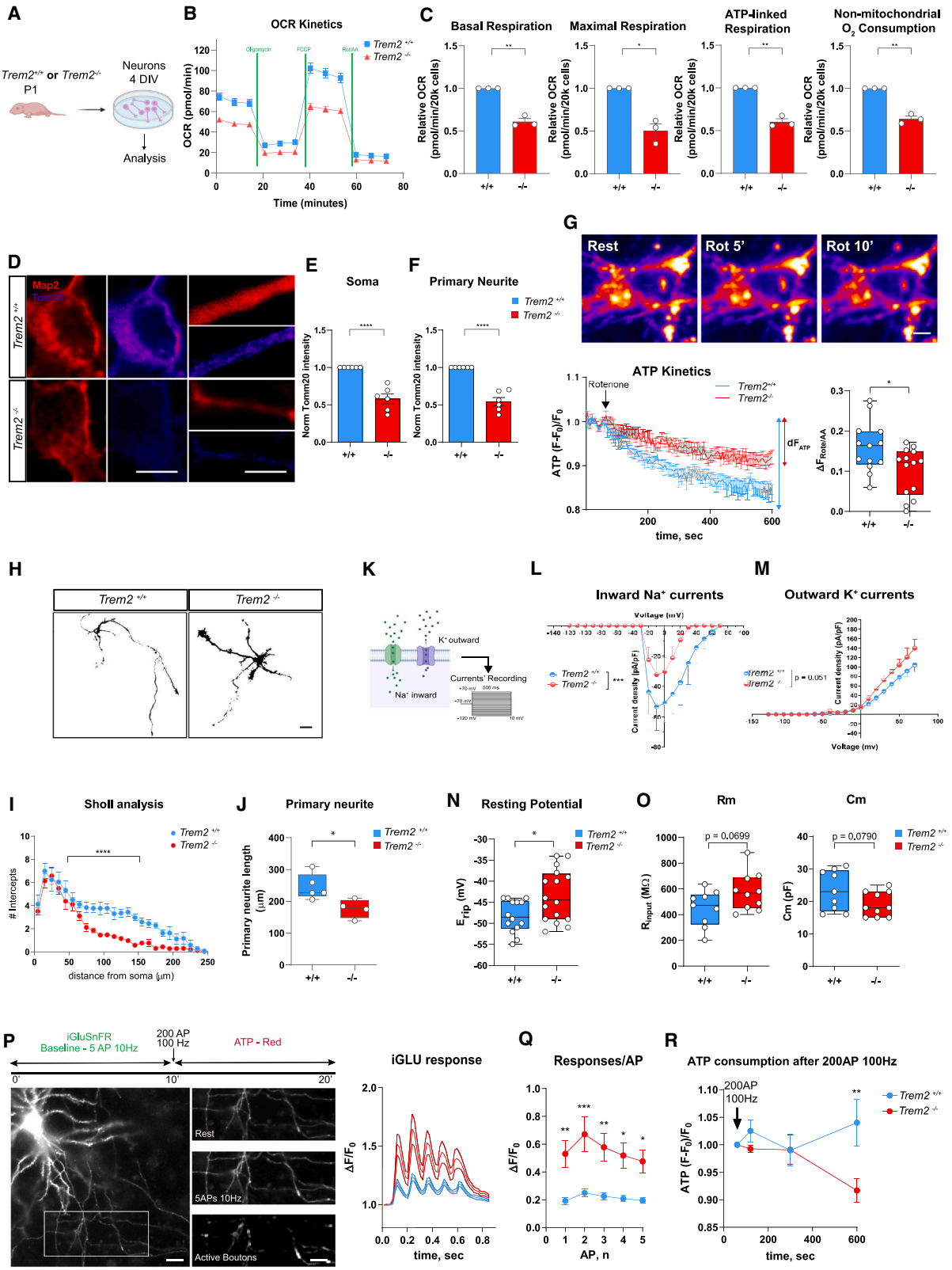

Figure 7. Trem2$^{-/-}$ neurons display mitochondrial defects and faulty differentiation in culture

(A) Cartoon showing the experimental design.

(B) Average OCR kinetics showing the response of 4 DIV *Trem2*$^{+/+}$ or *Trem2*$^{-/-}$ primary hippocampal neurons to different mitochondrial inhibitors.

(legend continued on next page)

(Figures S5A–S5C). Furthermore, live-imaging recordings at synaptic boutons of 14 DIV *Trem2*$^{-/-}$ synapses, using the glutamate sensing fluorescent reporter (iGluSNFR), revealed a significant increase in glutamate release, compared with control cultures (Figures 7P and 7Q). To evaluate the dependency of these synapses on mitochondrial ATP, we recorded, from the very same synapses, the fluctuation in mitochondrial ATP in response to high-frequency stimulation and the synaptic ATP fluctuations using ATP-red dye and found that *Trem2*$^{-/-}$ synapses fail to produce ATP in response to high-frequency stimulation (Figure 7R), in line with reduced mitochondrial functionality.

To start evaluating whether the defective metabolic phenotype of neurons developing in the absence of microglial *Trem2* could result from the early neuronal exposure to an altered microglial secretome,[69–72] pre-conditioned medium (CM) harvested from either *Trem2*$^{+/+}$ or *Trem2*$^{-/-}$ primary microglia was applied to primary neurons isolated from *Trem2*$^{+/+}$ or *Trem2*$^{-/-}$ hippocampi and maintained for 4 DIV (Figure S7F). Seahorse experiments (Figure S7G) revealed defective metabolic parameters in *Trem2*$^{-/-}$ as compared with *Trem2*$^{+/+}$ neurons. However, released soluble factors did not boost any of the metabolic parameters (Figures S7H–S7K), with a very modest, not significant, effect of the supernatant, regardless of whether it was derived from *Trem2*$^{+/+}$ or *Trem2*$^{-/-}$ microglia.

Taken together, these results indicate that the lack of Trem2-mediated communication between microglia and neurons during early developmental windows is sufficient to derange the forthcoming neuronal metabolism and mitochondria organization, which is maintained in neurons even after their isolation from the brain context. These defects are associated with a delay in the maturation of *Trem2*$^{-/-}$ neurons, followed, both *ex vivo* and *in vitro*, by dysregulated glutamatergic neurotransmission. Furthermore, the secretome from *Trem2*$^{+/+}$ microglia is not able to revert the defective metabolic profile of neurons, suggesting that more structured bidirectional microglia-neuron communication may be required.

DISCUSSION

Microglia are highly dynamic cells that patrol brain parenchyma, sensing the neuronal activity and regulating neuronal functions through the release of a wide spectrum of immunoregulatory factors. Through secretory and cell-to-cell contact-mediated processes, microglia dynamically regulate neuronal development, growth, formation of synapses, and physiological functions of brain cells.[1,73] We have previously demonstrated that lack of the immune receptor Trem2 results in microglia's inability to properly perform supernumerary synapse elimination during brain development.[43] Also, we have shown that adult (P90) Trem2-deficient mice display altered brain connectivity and behavioral defects.[43,45] We now demonstrate that *Trem2* deficiency impairs neuronal transcriptomic and energetic profile, suggesting that early metabolic derangements in neurons may contribute to connectivity and behavioral defects occurring in adult *Trem2*$^{-/-}$ mice.

Lack of *Trem2* strongly impacts the expression of EIF2 signaling in neurons, which is heavily downregulated in CA-ImmPyr and upregulated in CA1-Pyr and CA3-Pyr. By controlling the eIF2.GTP.Met-tRNAiMet ternary complexes, EIF2 activity governs the rate of global translation, and its phosphorylation is recognized as implicated in nervous system development and memory consolidation.[74,75] Indeed, genetic reduction of

(C) From left to right: basal, maximal, ATP-coupled respiration, and non-mitochondrial oxygen consumption rates. Mean ± SEM of n = 25 replicates from N = 3 independent *Trem2*$^{+/+}$ and *Trem2*$^{-/-}$ cultures. One sample t test, ****p < 0.0001.
(D) Confocal images of 4 DIV *Trem2*$^{+/+}$ or *Trem2*$^{-/-}$ primary hippocampal neurons labeled with Abs against Tom20 (fire look-up table [LUT]) and MAP2 (red). Scale bars, 8 and 4 μm.
(E and F) Tom20 mean intensity at somata (E) and primary neurites (F), respectively. Mean ± SEM of n = 40 (*Trem2*$^{+/+}$) and n = 40 (*Trem2*$^{-/-}$) neurons from N = 6 independent *Trem2*$^{+/+}$ and *Trem2*$^{-/-}$ neuronal cultures. Unpaired t test, ****p < 0.0001.
(G) Up: representative ATP-red fluorescence variation upon pharmacological inhibition of mitochondrial complex 1 and 3 (rotenone/AA) in 4 DIV *Trem2*$^{+/+}$ neuronal somata. Scale bars, 2 μm. Down left: average ATP-red traces at soma ($\Delta F/F_0$). Data are presented as mean ± SEM. Down right: plots showing ATP reduction after 15 min from the treatment ($\Delta F_{Rote/AA}$). Box-and-whiskers plots of n = 13 (*Trem2*$^{+/+}$) and n = 14 (*Trem2*$^{-/-}$) neurons from N = 4 *Trem2*$^{+/+}$ and *Trem2*$^{-/-}$ neuronal cultures. Unpaired Student's t test, *p < 0.05.
(H) Confocal images of 4 DIV *Trem2*$^{+/+}$ or *Trem2*$^{-/-}$ primary hippocampal neurons labeled with Ab against MAP2 and processed for Sholl analysis. Scale bars, 20 μm.
(I) Mean arborization of 4 DIV *Trem2*$^{+/+}$ or *Trem2*$^{-/-}$ primary hippocampal neurons. Mean ± SEM of n = 54 (*Trem2*$^{+/+}$) and n = 41 (*Trem2*$^{-/-}$) neurons from N = 5 independent *Trem2*$^{+/+}$ or N = 4 *Trem2*$^{-/-}$ primary neuronal cultures. Two-way ANOVA followed by Sidak's multi-comparison test, ****p < 0.0001.
(J) Primary neurite length in 4 DIV *Trem2*$^{+/+}$ or *Trem2*$^{-/-}$ primary hippocampal neurons. Box-and-whiskers plots of n = 54 (*Trem2*$^{+/+}$) and 41 (*Trem2*$^{-/-}$) neurons from independent N = 5 *Trem2*$^{+/+}$ or N = 4 *Trem2*$^{-/-}$ primary neuronal cultures. Unpaired t test, *p < 0.05.
(K) Cartoon of the experimental design.
(L and M) Mean inward Na^+ and outward K^+ currents of 4 DIV *Trem2*$^{+/+}$ or *Trem2*$^{-/-}$ primary hippocampal neurons. n = 5–10 (*Trem2*$^{+/+}$) and n = 6–9 (*Trem2*$^{-/-}$) neurons from N = 3 *Trem2*$^{+/+}$ or *Trem2*$^{-/-}$ primary neuronal cultures. Two-way ANOVA, ***p < 0.001.
(N) Resting potential of 4 DIV *Trem2*$^{+/+}$ or *Trem2*$^{-/-}$ primary hippocampal neurons. Box-and-whiskers plots of n = 14 (*Trem2*$^{+/+}$) and n = 16 (*Trem2*$^{-/-}$) neurons from N = 4 *Trem2*$^{+/+}$ or *Trem2*$^{-/-}$ primary neuronal cultures. Mann-Whitney U test, *p < 0.05.
(O) Resistivity (left) and capacitance (right) values of 4 DIV *Trem2*$^{+/+}$ or *Trem2*$^{-/-}$ primary hippocampal neurons. Box-and-whiskers plots of n = 9 (*Trem2*$^{+/+}$) and n = 10 (*Trem2*$^{-/-}$) neurons from N = 3 *Trem2*$^{+/+}$ and *Trem2*$^{-/-}$ neuronal cultures. Unpaired t test.
(P) Up: description of the iGluSNFR live-imaging experimental design. Down: representative iGluSNFR fluorescence images in a transfected *Trem2*$^{+/+}$ neuron. Zoomed image of an axonal branch with active synaptic boutons after a 10-Hz stimulation of 5 APs. Scale bars, 20 and 5 μm. Left: average traces of iGluSNFR response to 5 APs at 10 Hz in *Trem2*$^{+/+}$ and *Trem2*$^{-/-}$ synapses. Mean ± SEM of n = 22 (*Trem2*$^{+/+}$) and or n = 21 (*Trem2*$^{-/-}$) coverslips from N = 5–6 hippocampal cultures from P1 *Trem2*$^{+/+}$ or *Trem2*$^{-/-}$ pups.
(Q) $\Delta F/F_0$ response in relation to AP number. Two-way ANOVA followed by Sidak's multi-comparison test, *p < 0.05, **p < 0.01, and ***p < 0.001.
(R) Average traces of ATP-red fluorescence time course after 200 APs at 100 Hz in *Trem2*$^{+/+}$ or *Trem2*$^{-/-}$ synapses. Two-way ANOVA followed by Sidak's multi-comparison test, **p < 0.01.

Elf2b activity induces delayed post-natal brain development, abnormal glial cell abundance, increased abundance of demyelinated axons, and impaired cerebral inflammatory response upon insults.[76,77]

In this study, we provide several lines of evidence indicating that mitochondrial and energetic assets of CA1 neurons are profoundly altered in the absence of microglial Trem2. Microglia react to the environment by flexibly reprogramming their metabolic pathways, in a process called immunometabolism.[78,79] Indeed, while homeostatic microglia mostly rely upon OXPHOS for ATP production, inflammatory microglia reprogram their metabolism toward aerobic glycolysis.[80–82] Further, Trem2 plays a key role in modulating cellular biosynthetic metabolism[16] and is centrally involved in inducing transcriptomic and functional programs of DAMs, a phagocytic state detected in the brain during neurodegeneration.[26,33]

We found that in the early post-natal period microglia equally rely on glycolysis and OXPHOS for ATP supply. We also showed that, in line with the central role of Trem2 in the control of microglia metabolism,[16] the lack of the gene causes, at birth, a reduction in mitochondrial mass without, however, major changes in the OCR. Conversely, hippocampal neurons from *Trem2*$^{-/-}$ mice displayed impaired mitochondrial metabolism, with selective deterioration in the basal, maximal, and ATP-coupled respiration, accompanied by diminished mitochondrial mass and reduced mitochondria length. Thus, the lack of microglial *Trem2* predominantly affects neuronal metabolic properties.

Differently from microglia, neurons are allowed only a limited degree of metabolic flexibility, which is required to ensure fate stability and sustained cellular functionality. During development, a continuous metabolic glycolytic rewiring of stem and precursor cells allows cell fate regulation, proliferation, and differentiation processes. Conversely, mature neurons, to prioritize network maintenance, mostly rely on OXPHOS and mitochondria, with a very minor proportion of their energy deriving from glycolytic processes[83] deputed to the control of processes such as synaptic vesicle trafficking.[84] It has been proposed that glycolysis or certain glycolytic metabolites are incompatible with neuronal identity and survival,[83] causing neural cell dedifferentiation, loss of cell fate stability, defects in synaptic transmission, and ultimately, cell death. In line with the metabolic switch from glycolysis to OXPHOS representing an essential step in neuronal maturation, defects in the OXPHOS genes contribute toward neurodevelopmental disorders.[85,86] The neuronal reduction in OXPHOS observed in *Trem2*$^{-/-}$ mice likely represents an impasse to proper neuronal and synapse maturation and possibly even to brain circuit development.

We showed that the delayed CA1 pyramidal neuron maturation in *Trem2*$^{-/-}$ mice is followed at P18 by the enhancement of excitatory neurotransmission. A similar phenomenon has been reported in different neurodevelopmental disorders, such as Rett syndrome, Down syndrome, and epileptic encephalopathies, where brain energy dysfunctions are associated with neuronal developmental delay and followed by an increase in excitatory transmission,[87,88] correlating with enhanced network synchronicity.[65,89] Furthermore, the ATP produced by glycolysis, but not mitochondria, is harnessed for glutamate accumulation into synaptic vesicles.[90] These data provide a logical frame to our observation that *Trem2*$^{-/-}$ neurons, which are defective in mitochondrial respiration, release a higher amount of glutamate upon stimulation. At later stages of brain maturation (P90), *Trem2*$^{-/-}$ mice display an impoverishment of hippocampal synaptic markers,[43] which specifically occurs in the CA1 region. This event associates with altered functional connectivity and significant defects in circuit maturation.[43,45] Thus, *Trem2*$^{-/-}$ mice seem unable to properly build and strengthen the correct synaptic setup during brain maturation, as a possible result of the neuronal metabolic impairment as well as the defective synapse elimination during the period of synaptic pruning.

Ample evidence has recently implicated mitochondria in early brain development. Mitochondria function is associated with neurogenesis, differentiation, and maturation of neurons. During mid-corticogenesis, mitochondria assembly, fusion/fission, and mobility dynamics are key processes that warrant progenitors' self-renewal capability and maintenance.[57–59] Alterations of the timing in the fusion/fission paradigm affect neurogenesis,[91] and defects in mitochondria mobility and energy metabolism selectively impinge on neuronal differentiation and migration of cortical interneurons[92] Moreover, mitochondrial biogenesis is critical for spine formation and maintenance in hippocampal neurons.[93] To our knowledge, only cell-autonomous mechanisms have been so far identified in underpinning neuronal metabolic programs. In this study, we show a role for microglia in controlling neuronal maturation and metabolic fitness and identify Trem2 signaling as an early potential modulator of such microglia-neuron crosstalk.

Beyond DG neurons, we detected a selective vulnerability of specific classes of neurons and identify CA1 neurons as one of the neuronal subtypes most susceptible to the lack of Trem2. Consistently, mitochondrial defects and metabolic derangements occur specifically—and are even exacerbated at later (P18) developmental stages—in the CA1 and not the CA3 region. Consistently, assessment of the neuronal developmental trajectories in newborn mouse hippocampus by pseudotime analysis revealed a clear shift in the metabolic signature of CA1 neurons, associated with a delay in neuronal maturation. We have previously shown that also synaptic pruning depends on Trem2 predominantly in the CA1 as compared with the CA3 region.[43] Thus, several Trem2 functions are achieved in a region-dependent manner. Although the basis for the selective susceptibility of the CA1 region to *Trem2*-depletion is not fully defined, it is relevant that CA1 microglia express higher *Trem2*. Furthermore, even partial reductions of *Trem2* expression, as in *Trem2* hemizygous mice, are sufficient to derange CA1 pyramidal neuron metabolism, indicating that the CA1 requires high microglial Trem2 to properly control pyramidal neuron differentiation. These data have important implications, opening the possibility that conditions characterized by reduced *Trem2*, including *Trem2* hemizygous missense variants in patients,[34,38,94] may suffer from neuronal metabolic dysfunctions.

How Trem2 modulates microglia-neuron communication remains to be defined. One possibility is that the lack of *Trem2* and consequent modification of the microglial state could result in altered secretome, which in turn would differentially affect neuronal trajectories. Alternatively, or concomitantly, microglia-to-neuron contacts occurring during early development may play a role. Specifically, Trem2 localized at the microglial membrane could bind to immature neuronal partners, influencing their

metabolic trajectories. It has been found that throughout embryonic and adult neurogenesis, microglial processes can form specialized contacts with the cell bodies of developing neurons, characterized by the clustering of functional microglial P2yr12 receptors and enriched with mitochondria.[95] In the absence of microglial P2yr12, erratic cortical cytoarchitecture occurs and is maintained in adulthood.[95,96] The selective effect on excitatory cells, which are born locally in the hippocampus, where all the developing stages are potentially in contact with instructive microglia, is in line with the possibility of a cell-to-cell contact-dependent mechanism. Our pseudotime analysis suggests that this putative interaction, occurring at early stages of maturation of the neuronal excitatory lineage, may exert a potential ''priming'' effect, possibly differently in CA1 vs. CA3 regions, where *Trem2* is expressed at a different extent.

At present, we do not know whether microglia control the neuronal metabolic maturation only during development or are also active in different temporal windows. Neuronal changes in glucose metabolism occur during aging, when senescent neurons exhibit mitochondrial dysfunctions and increase their capability to oxidize glucose via glycolysis.[97] A reduction in Trem2 expression also occurs during senescence,[98] suggesting that these two mechanisms might contribute to the neuronal metabolic switch from OXPHOS to glycolysis during aging. Indeed, *Trem2*$^{-/-}$ mouse brains analyzed by fluoro-2-deoxy-d-glucose micro positron emission tomography (FDG-μPET) display reduced glucose metabolism,[99] while a knockin mouse model for the disease-associated *Trem2* T66M mutation presents a significant reduction in both microglial activity and overall brain glucose metabolism.[38] Although the total FDG uptake measured by PET is the composite of neuronal, astroglial, and microglial cells' metabolic profiles, it is possible that a crosstalk, like that occurring between microglia and neurons during early development, might be operative also during aging, and whenever compromised, it contributes to neurodegeneration. In this respect, it is particularly relevant that one of the functional consequences of the lack of *Trem2* is the increase in glutamate release and spontaneous neuronal activity. It is known for many years that the hippocampus is importantly affected in AD[100] and that an increase in hyperactive neurons in the CA1 region occurs before the formation of plaques.[101,102] Also, thinning of the CA1 apical neuropil occurs in subjects with mild AD, compared with controls,[103] while at later stages the CA1 region suffers more severe synaptic alterations.[104] Importantly, we show that adult (P90) *Trem2*$^{-/-}$ mice are characterized by a significant synaptic impoverishment, which occurs selectively in the CA1 region and accompanies the connectomic and behavioral deficits already described.[43,45] Thus, the possibility that a faulty control of neuronal metabolism by defective microglial *Trem2* results in deranged neuronal activity also during aging and neurodegeneration is a scenario worth investigating.

Limitations of the study

Although revealing a new role of TREM2 in early neurodevelopment, our study still lacks in identifying the molecular mechanisms by which Trem2-bearing microglia control the metabolic neuronal fate. More detailed analyses should be performed, addressing the possible roles of sTrem2 or microglia-derived extracellular vesicles[105] and identifying the molecular code of the microglia-to-neuron communication, including whether CA1 and CA3 regions differently express putative Trem2 interactors. Furthermore, experiments of microglial Trem2 expression down-regulation in early post-natal windows would univocally prove that the synaptic and circuits defects observed in the adult mouse result from a microglia-to-neuron crosstalk dysregulation occurring during the early development. Moreover, since the lack of Trem2 impairs both synapse refinement[43] and neuronal metabolism (this study), it would be important in the future to define next at which extent the two processes relatively contribute to the synaptic setup during brain maturation.

STAR★METHODS

Detailed methods are provided in the online version of this paper and include the following:

- KEY RESOURCES TABLE
- RESOURCE AVAILABILITY
  - Lead contact
  - Materials availability
  - Data and Code availability
- METHOD DETAILS
  - Mice
  - Primary hippocampal neuronal culture and transfection
  - Primary microglia culture
  - Live-imaging experiments
  - RNAseq analysis
  - Electrophysiology
  - Immunofluorescence analysis
  - Electron microscopy

SUPPLEMENTAL INFORMATION

Supplemental information can be found online at https://doi.org/10.1016/j.immuni.2023.12.002.

ACKNOWLEDGMENTS

We thank Prof. K. Volynski (Department of Experimental and Clinical Epilepsy) for kindly providing iGluSnFR and GFP plasmids. We thank C. Ferrari, D. Pozzi, E. Fraviga, C.A. Elia, and C. Saulle for help in setting up experimental methodologies. The present work was supported by ERC AdG MATILDA 101055323, EraNET Neuron JTC2021 InflASD and Telethon GGP20030 to M.M., by ERC StG IMPACT 101043003, Cariplo Giovani 2019-1785 to S.L., by a Grant D.R. 3404 on Heavy Equipment, HITACHI 120 kV TEM microscope HT7800 to K.C. E.T. and A.C. are supported by a High Profile PostDoctoral (HiPPO) Fellowship by Fondazione Humanitas per la Ricerca. Cartoons and GA have been created with Biorender.com.

AUTHOR CONTRIBUTIONS

E.T. performed primary neuronal and microglia cultures; performed and analyzed *in vitro* live-imaging experiments, *ex vivo* electron microscopy, and *in vitro* and *ex vivo* immunofluorescence experiments; and assisted in sample collection. G.D. performed primary neuronal cultures, performed and analyzed *in vitro* and *ex vivo* Seahorse experiments, and assisted in sample collection. M.B. performed primary microglia cultures, immunofluorescence experiments, conditioned media preparation, and sample collection. E.F. performed qPCR, colony maintenance, genotyping, and sample collection. A.C., R.J.A., and G.D. designed and A.C. performed SCENITH experiments. F.F. and A.C. set up and performed FACS experiments. S.M., M.M., and S.L.

performed, analyzed, and interpreted the single-cell sequencing data. M.C.G. and K.C. performed and analyzed *ex vivo* electron microscopy. R.M. performed *in vitro* electrophysiological recordings, immunofluorescence experiments, and assisted in sample preparation. R.H.-S. performed MEA recordings, and P.P. performed *ex vivo* immunofluorescence experiments. M.M., E.T., G.D., and R.M. conceived the study, designed the experiments, and analyzed the data. M.M., E.T., G.D., and S.L. wrote the original draft of the manuscript, and all authors revised the manuscript.

DECLARATION OF INTERESTS

The authors declare no competing interests.

Received: September 15, 2022
Revised: July 17, 2023
Accepted: December 5, 2023
Published: December 29, 2023

REFERENCES

1. Colonna, M., and Butovsky, O. (2017). Microglia function in the central nervous system during health and neurodegeneration. Annu. Rev. Immunol. *35*, 441–468.
2. Hammond, T.R., Dufort, C., Dissing-Olesen, L., Giera, S., Young, A., Wysoker, A., Walker, A.J., Gergits, F., Segel, M., Nemesh, J., et al. (2019). Single-cell RNA sequencing of microglia throughout the mouse lifespan and in the injured brain reveals complex cell-state changes. Immunity *50*, 253–271.e6.
3. Hughes, A.N., and Appel, B. (2020). Microglia phagocytose myelin sheaths to modify developmental myelination. Nat. Neurosci. *23*, 1055–1066.
4. Paolicelli, R.C., Bolasco, G., Pagani, F., Maggi, L., Scianni, M., Panzanelli, P., Giustetto, M., Ferreira, T.A., Guiducci, E., Dumas, L., et al. (2011). Synaptic pruning by microglia is necessary for normal brain development. Science *333*, 1456–1458.
5. Paolicelli, R.C., Sierra, A., Stevens, B., Tremblay, M.E., Aguzzi, A., Ajami, B., Amit, I., Audinat, E., Bechmann, I., Bennett, M., et al. (2022). Microglia states and nomenclature: a field at its crossroads. Neuron *110*, 3458–3483.
6. Schafer, D.P., Lehrman, E.K., Kautzman, A.G., Koyama, R., Mardinly, A.R., Yamasaki, R., Ransohoff, R.M., Greenberg, M.E., Barres, B.A., and Stevens, B. (2012). Microglia sculpt postnatal neural circuits in an activity and complement-dependent manner. Neuron *74*, 691–705.
7. Sierra, A., Encinas, J.M., Deudero, J.J.P., Chancey, J.H., Enikolopov, G., Overstreet-Wadiche, L.S., Tsirka, S.E., and Maletic-Savatic, M. (2010). Microglia shape adult hippocampal neurogenesis through apoptosis-coupled phagocytosis. Cell Stem Cell *7*, 483–495.
8. Thion, M.S., Ginhoux, F., and Garel, S. (2018). Microglia and early brain development: an intimate journey. Science *362*, 185–189.
9. Zhan, Y., Paolicelli, R.C., Sforazzini, F., Weinhard, L., Bolasco, G., Pagani, F., Vyssotski, A.L., Bifone, A., Gozzi, A., Ragozzino, D., et al. (2014). Deficient neuron-microglia signaling results in impaired functional brain connectivity and social behavior. Nat. Neurosci. *17*, 400–406.
10. Colonna, M. (2023). The biology of TREM receptors. Nat. Rev. Immunol. *23*, 580–594.
11. Kiialainen, A., Hovanes, K., Paloneva, J., Kopra, O., and Peltonen, L. (2005). Dap12 and Trem2, molecules involved in innate immunity and neurodegeneration, are co-expressed in the CNS. Neurobiol. Dis. *18*, 314–322.
12. Neumann, H., and Takahashi, K. (2007). Essential role of the microglial triggering receptor expressed on myeloid cells-2 (TREM2) for central nervous tissue immune homeostasis. J. Neuroimmunol. *184*, 92–99.
13. Schmid, C.D., Sautkulis, L.N., Danielson, P.E., Cooper, J., Hasel, K.W., Hilbush, B.S., Sutcliffe, J.G., and Carson, M.J. (2002). Heterogeneous expression of the triggering receptor expressed on myeloid cells-2 on adult murine microglia. J. Neurochem. *83*, 1309–1320.
14. Takahashi, K., Rochford, C.D.P., and Neumann, H. (2005). Clearance of apoptotic neurons without inflammation by microglial triggering receptor expressed on myeloid cells-2. J. Exp. Med. *201*, 647–657.
15. Turnbull, I.R., Gilfillan, S., Cella, M., Aoshi, T., Miller, M., Piccio, L., Hernandez, M., and Colonna, M. (2006). Cutting edge: TREM-2 attenuates macrophage activation. J. Immunol. *177*, 3520–3524.
16. Ulland, T.K., Song, W.M., Huang, S.C.-C., Ulrich, J.D., Sergushichev, A., Beatty, W.L., Loboda, A.A., Zhou, Y., Cairns, N.J., Kambal, A., et al. (2017). TREM2 maintains microglial metabolic fitness in Alzheimer's disease. Cell *170*, 649–663.e13.
17. Filipello, F., You, S.F., Mirfakhar, F.S., Mahali, S., Bollman, B., Acquarone, M., Korvatska, O., Marsh, J.A., Sivaraman, A., Martinez, R., et al. (2023). Defects in lysosomal function and lipid metabolism in human microglia harboring a TREM2 loss of function mutation. Acta Neuropathol. *145*, 749–772.
18. Nugent, A.A., Lin, K., van Lengerich, B., Lianoglou, S., Przybyla, L., Davis, S.S., Llapashtica, C., Wang, J., Kim, D.J., Xia, D., et al. (2020). TREM2 regulates microglial cholesterol metabolism upon chronic phagocytic challenge. Neuron *105*, 837–854.e9.
19. van Lengerich, B., Zhan, L., Xia, D., Chan, D., Joy, D., Park, J.I., Tatarakis, D., Calvert, M., Hummel, S., Lianoglou, S., et al. (2023). A TREM2-activating antibody with a blood–brain barrier transport vehicle enhances microglial metabolism in Alzheimer's disease models. Nat. Neurosci. *26*, 416–429.
20. Wang, S., Sudan, R., Peng, V., Zhou, Y., Du, S., Yuede, C.M., Lei, T., Hou, J., Cai, Z., Cella, M., et al. (2022). TREM2 drives microglia response to amyloid-β via SYK-dependent and -independent pathways. Cell *185*, 4153–4169.e19.
21. Cignarella, F., Filipello, F., Bollman, B., Cantoni, C., Locca, A., Mikesell, R., Manis, M., Ibrahim, A., Deng, L., Benitez, B.A., et al. (2020). TREM2 activation on microglia promotes myelin debris clearance and remyelination in a model of multiple sclerosis. Acta Neuropathol. *140*, 513–534.
22. Kober, D.L., and Brett, T.J. (2017). TREM2-ligand interactions in health and disease. J. Mol. Biol. *429*, 1607–1629.
23. Otero, K., Shinohara, M., Zhao, H., Cella, M., Gilfillan, S., Colucci, A., Faccio, R., Ross, F.P., Teitelbaum, S.L., Takayanagi, H., et al. (2012). TREM2 and β-catenin regulate bone homeostasis by controlling the rate of osteoclastogenesis. J. Immunol. *188*, 2612–2621.
24. Wang, Y., Cella, M., Mallinson, K., Ulrich, J.D., Young, K.L., Robinette, M.L., Gilfillan, S., Krishnan, G.M., Sudhakar, S., Zinselmeyer, B.H., et al. (2015). TREM2 lipid sensing sustains the microglial response in an Alzheimer's disease model. Cell *160*, 1061–1071.
25. Yeh, F.L., Wang, Y., Tom, I., Gonzalez, L.C., and Sheng, M. (2016). TREM2 binds to apolipoproteins, including APOE and CLU/APOJ, and thereby facilitates uptake of amyloid-beta by microglia. Neuron *91*, 328–340.
26. Keren-Shaul, H., Spinrad, A., Weiner, A., Matcovitch-Natan, O., Dvir-Szternfeld, R., Ulland, T.K., David, E., Baruch, K., Lara-Astaiso, D., Toth, B., et al. (2017). A unique microglia type associated with restricting development of Alzheimer's disease. Cell *169*, 1276–1290.e17.
27. Feuerbach, D., Schindler, P., Barske, C., Joller, S., Beng-Louka, E., Worringer, K.A., Kommineni, S., Kaykas, A., Ho, D.J., Ye, C., et al. (2017). ADAM17 is the main sheddase for the generation of human triggering receptor expressed in myeloid cells (hTREM2) ectodomain and cleaves TREM2 after histidine 157. Neurosci. Lett. *660*, 109–114.
28. Wunderlich, P., Glebov, K., Kemmerling, N., Tien, N.T., Neumann, H., and Walter, J. (2013). Sequential proteolytic processing of the triggering receptor expressed on myeloid cells-2 (TREM2) protein by ectodomain shedding and γ-secretase-dependent intramembranous cleavage. J. Biol. Chem. *288*, 33027–33036.
29. Del-Aguila, J.L., Benitez, B.A., Li, Z., Dube, U., Mihindukulasuriya, K.A., Budde, J.P., Farias, F.H.G., Fernández, M.V., Ibanez, L., Jiang, S., et al. (2019). TREM2 brain transcript-specific studies in AD and TREM2 mutation carriers. Mol. Neurodegener. *14*, 18.

30. Filipello, F., Goldsbury, C., You, S.F., Locca, A., Karch, C.M., and Piccio, L. (2022). Soluble TREM2: innocent bystander or active player in neurological diseases? Neurobiol. Dis. *165*, 105630.

31. Piccio, L., Buonsanti, C., Cella, M., Tassi, I., Schmidt, R.E., Fenoglio, C., Rinker, J., Naismith, R.T., Panina-Bordignon, P., Passini, N., et al. (2008). Identification of soluble TREM-2 in the cerebrospinal fluid and its association with multiple sclerosis and CNS inflammation. Brain *131*, 3081–3091.

32. Suárez-Calvet, M., Kleinberger, G., Araque Caballero, M.Á., Brendel, M., Rominger, A., Alcolea, D., Fortea, J., Lleó, A., Blesa, R., Gispert, J.D., et al. (2016). sTREM2 cerebrospinal fluid levels are a potential biomarker for microglia activity in early-stage Alzheimer's disease and associate with neuronal injury markers. EMBO Mol. Med. *8*, 466–476.

33. Deczkowska, A., Keren-Shaul, H., Weiner, A., Colonna, M., Schwartz, M., and Amit, I. (2018). Disease-associated microglia: a universal immune sensor of neurodegeneration. Cell *173*, 1073–1081.

34. Guerreiro, R., Wojtas, A., Bras, J., Carrasquillo, M., Rogaeva, E., Majounie, E., Cruchaga, C., Sassi, C., Kauwe, J.S.K., Younkin, S., et al. (2013). TREM2 variants in Alzheimer's disease. N. Engl. J. Med. *368*, 117–127.

35. Jin, S.C., Benitez, B.A., Karch, C.M., Cooper, B., Skorupa, T., Carrell, D., Norton, J.B., Hsu, S., Harari, O., Cai, Y., et al. (2014). Coding variants in TREM2 increase risk for Alzheimer's disease. Hum. Mol. Genet. *23*, 5838–5846.

36. Jonsson, T., Stefansson, H., Steinberg, S., Jonsdottir, I., Jonsson, P.V., Snaedal, J., Bjornsson, S., Huttenlocher, J., Levey, A.I., Lah, J.J., et al. (2013). Variant of TREM2 associated with the risk of Alzheimer's disease. N. Engl. J. Med. *368*, 107–116.

37. Yeh, F.L., Hansen, D.V., and Sheng, M. (2017). TREM2, microglia, and neurodegenerative diseases. Trends Mol. Med. *23*, 512–533.

38. Kleinberger, G., Yamanishi, Y., Suárez-Calvet, M., Czirr, E., Lohmann, E., Cuyvers, E., Struyfs, H., Pettkus, N., Wenninger-Weinzierl, A., Mazaheri, F., et al. (2014). TREM2 mutations implicated in neurodegeneration impair cell surface transport and phagocytosis. Sci. Transl. Med. *6*, 243ra86.

39. Krasemann, S., Madore, C., Cialic, R., Baufeld, C., Calcagno, N., El Fatimy, R., Beckers, L., O'Loughlin, E., Xu, Y., Fanek, Z., et al. (2017). The TREM2-APOE pathway drives the transcriptional phenotype of dysfunctional microglia in neurodegenerative diseases. Immunity *47*, 566–581.e9.

40. Yuan, P., Condello, C., Keene, C.D., Wang, Y., Bird, T.D., Paul, S.M., Luo, W., Colonna, M., Baddeley, D., and Grutzendler, J. (2016). TREM2 haplodeficiency in mice and humans impairs the microglia barrier function leading to decreased amyloid compaction and severe axonal dystrophy. Neuron *90*, 724–739.

41. Cantoni, C., Bollman, B., Licastro, D., Xie, M., Mikesell, R., Schmidt, R., Yuede, C.M., Galimberti, D., Olivecrona, G., Klein, R.S., et al. (2015). TREM2 regulates microglial cell activation in response to demyelination in vivo. Acta Neuropathol. *129*, 429–447.

42. Dong, Y., D'Mello, C., Pinsky, W., Lozinski, B.M., Kaushik, D.K., Ghorbani, S., Moezzi, D., Brown, D., Melo, F.C., Zandee, S., et al. (2021). Oxidized phosphatidylcholines found in multiple sclerosis lesions mediate neurodegeneration and are neutralized by microglia. Nat. Neurosci. *24*, 489–503.

43. Filipello, F., Morini, R., Corradini, I., Zerbi, V., Canzi, A., Michalski, B., Erreni, M., Markicevic, M., Starvaggi-Cucuzza, C., Otero, K., et al. (2018). The microglial innate immune receptor TREM2 is required for synapse elimination and normal brain connectivity. Immunity *48*, 979–991.e8.

44. Scott-Hewitt, N., Perrucci, F., Morini, R., Erreni, M., Mahoney, M., Witkowska, A., Carey, A., Faggiani, E., Schuetz, L.T., Mason, S., et al. (2020). Local externalization of phosphatidylserine mediates developmental synaptic pruning by microglia. EMBO J. *39*, e105380.

45. Zerbi, V., Pagani, M., Markicevic, M., Matteoli, M., Pozzi, D., Fagiolini, M., Bozzi, Y., Galbusera, A., Scattoni, M.L., Provenzano, G., et al. (2021). Brain mapping across 16 autism mouse models reveals a spectrum of functional connectivity subtypes. Mol. Psychiatry *26*, 7610–7620.

46. Chertoff, M., Shrivastava, K., Gonzalez, B., Acarin, L., and Giménez-Llort, L. (2013). Differential modulation of TREM2 protein during postnatal brain development in mice. PLoS One *8*, e72083.

47. Thrash, J.C., Torbett, B.E., and Carson, M.J. (2009). Developmental regulation of TREM2 and DAP12 expression in the murine CNS: implications for Nasu-Hakola disease. Neurochem. Res. *34*, 38–45.

48. Herst, P.M., Tan, A.S., Scarlett, D.J., and Berridge, M.V. (2004). Cell surface oxygen consumption by mitochondrial gene knockout cells. Biochim. Biophys. Acta *1656*, 79–87.

49. Argüello, R.J., Combes, A.J., Char, R., Gigan, J.P., Baaziz, A.I., Bousiquot, E., Camosseto, V., Samad, B., Tsui, J., Yan, P., et al. (2020). SCENITH: a flow cytometry-based method to functionally profile energy metabolism with single-cell resolution. Cell Metab. *32*, 1063–1075.e7.

50. Buttgereit, F., and Brand, M.D. (1995). A hierarchy of ATP-consuming processes in mammalian cells. Biochem. J. *312*, 163–167.

51. Aviner, R. (2020). The science of puromycin: from studies of ribosome function to applications in biotechnology. Comput. Struct. Biotechnol. J. *18*, 1074–1083.

52. Rangaraju, V., Lauterbach, M., and Schuman, E.M. (2019). Spatially stable mitochondrial compartments fuel local translation during plasticity. Cell *176*, 73–84.e15.

53. Hidalgo San Jose, L., and Signer, R.A.J. (2019). Cell-type-specific quantification of protein synthesis in vivo. Nat. Protoc. *14*, 441–460.

54. Mancinelli, S., and Lodato, S. (2018). Decoding neuronal diversity in the developing cerebral cortex: from single cells to functional networks. Curr. Opin. Neurobiol. *53*, 146–155.

55. La Manno, G., Soldatov, R., Zeisel, A., Braun, E., Hochgerner, H., Petukhov, V., Lidschreiber, K., Kastriti, M.E., Lönnerberg, P., Furlan, A., et al. (2018). RNA velocity of single cells. Nature *560*, 494–498.

56. Dann, E., Henderson, N.C., Teichmann, S.A., Morgan, M.D., and Marioni, J.C. (2022). Differential abundance testing on single-cell data using k-nearest neighbor graphs. Nat. Biotechnol. *40*, 245–253.

57. Brunetti, D., Dykstra, W., Le, S., Zink, A., and Prigione, A. (2021). Mitochondria in neurogenesis: implications for mitochondrial diseases. Stem Cells *39*, 1289–1297.

58. Iwata, R., Casimir, P., Erkol, E., Boubakar, L., Planque, M., Gallego López, I.M., Ditkowska, M., Gaspariunaite, V., Beckers, S., Remans, D., et al. (2023). Mitochondria metabolism sets the species-specific tempo of neuronal development. Science *379*, eabn4705.

59. Knobloch, M., and Jessberger, S. (2017). Metabolism and neurogenesis. Curr. Opin. Neurobiol. *42*, 45–52.

60. Asgarian, Z., Magno, L., Ktena, N., Harris, K.D., and Kessaris, N. (2019). Hippocampal CA1 somatostatin interneurons originate in the embryonic MGE/POA. Stem Cell Rep. *13*, 793–802.

61. Save, L., Baude, A., and Cossart, R. (2019). Temporal embryonic origin critically determines cellular physiology in the dentate gyrus. Cereb. Cortex *29*, 2639–2652.

62. Roche, M.E., Lin, Z., Whitaker-Menezes, D., Zhan, T., Szuhai, K., Bovee, J.V.M.G., Abraham, J.A., Jiang, W., Martinez-Outschoorn, U., and Basu-Mallick, A. (2020). Translocase of the outer mitochondrial membrane complex subunit 20 (TOMM20) facilitates cancer aggressiveness and therapeutic resistance in chondrosarcoma. Biochim. Biophys. Acta Mol. Basis Dis. *1866*, 165962.

63. Heine, K.B., and Hood, W.R. (2020). Mitochondrial behaviour, morphology, and animal performance. Biol. Rev. Camb. Philos. Soc. *95*, 730–737.

64. Chen, H., and Chan, D.C. (2009). Mitochondrial dynamics-fusion, fission, movement, and mitophagy-in neurodegenerative diseases. Hum. Mol. Genet. *18*, R169–R176.

65. Stampanoni Bassi, M., Iezzi, E., Gilio, L., Centonze, D., and Buttari, F. (2019). Synaptic plasticity shapes brain connectivity: implications for network topology. Int. J. Mol. Sci. *20*.

66. Song, M., Mohamad, O., Chen, D., and Yu, S.P. (2013). Coordinated development of voltage-gated Na+ and K+ currents regulates functional maturation of forebrain neurons derived from human induced pluripotent stem cells. Stem Cells Dev. *22*, 1551–1563.

67. Luhmann, H.J., Reiprich, R.A., Hanganu, I., and Kilb, W. (2000). Cellular physiology of the neonatal rat cerebral cortex: intrinsic membrane properties, sodium and calcium currents. J. Neurosci. Res. *62*, 574–584.

68. Spruston, N., and Johnston, D. (1992). Perforated patch-clamp analysis of the passive membrane properties of three classes of hippocampal neurons. J. Neurophysiol. *67*, 508–529.

69. Basso, M., and Bonetto, V. (2016). Extracellular vesicles and a novel form of communication in the brain. Front. Neurosci. *10*, 127.

70. Gabrielli, M., Raffaele, S., Fumagalli, M., and Verderio, C. (2022). The multiple faces of extracellular vesicles released by microglia: where are we 10 years after? Front. Cell. Neurosci. *16*, 984690.

71. Paolicelli, R.C., Bergamini, G., and Rajendran, L. (2019). Cell-to-cell communication by extracellular vesicles: focus on microglia. Neuroscience *405*, 148–157.

72. Rufino-Ramos, D., Albuquerque, P.R., Carmona, V., Perfeito, R., Nobre, R.J., and Pereira de Almeida, L. (2017). Extracellular vesicles: novel promising delivery systems for therapy of brain diseases. J. Control. Release *262*, 247–258.

73. Szepesi, Z., Manouchehrian, O., Bachiller, S., and Deierborg, T. (2018). Bidirectional microglia-neuron communication in health and disease. Front. Cell. Neurosci. *12*, 323.

74. Pavitt, G.D. (2005). eIF2B, a mediator of general and gene-specific translational control. Biochem. Soc. Trans. *33*, 1487–1492.

75. Bellato, H.M., and Hajj, G.N.M. (2016). Translational control by eIF2α in neurons: beyond the stress response. Cytoskeleton (Hoboken) *73*, 551–565.

76. Cabilly, Y., Barbi, M., Geva, M., Marom, L., Chetrit, D., Ehrlich, M., and Elroy-Stein, O. (2012). Poor cerebral inflammatory response in eIF2B knock-in mice: implications for the aetiology of vanishing white matter disease. PLoS One *7*, e46715.

77. Fogli, A., and Boespflug-Tanguy, O. (2006). The large spectrum of eIF2B-related diseases. Biochem. Soc. Trans. *34*, 22–29.

78. Hotamisligil, G.S. (2017). Foundations of immunometabolism and implications for metabolic health and disease. Immunity *47*, 406–420.

79. Makowski, L., Chaib, M., and Rathmell, J.C. (2020). Immunometabolism: from basic mechanisms to translation. Immunol. Rev. *295*, 5–14.

80. Cheng, J., Zhang, R., Xu, Z., Ke, Y., Sun, R., Yang, H., Zhang, X., Zhen, X., and Zheng, L.T. (2021). Early glycolytic reprogramming controls microglial inflammatory activation. J. Neuroinflammation *18*, 129.

81. Holland, R., McIntosh, A.L., Finucane, O.M., Mela, V., Rubio-Araiz, A., Timmons, G., McCarthy, S.A., Gun'ko, Y.K., and Lynch, M.A. (2018). Inflammatory microglia are glycolytic and iron retentive and typify the microglia in APP/PS1 mice. Brain Behav. Immun. *68*, 183–196.

82. Lauro, C., and Limatola, C. (2020). Metabolic reprograming of microglia in the regulation of the innate inflammatory response. Front. Immunol. *11*, 493.

83. Traxler, L., Lagerwall, J., Eichhorner, S., Stefanoni, D., D'Alessandro, A., and Mertens, J. (2021). Metabolism navigates neural cell fate in development, aging and neurodegeneration. Dis. Model. Mech. *14*, dmm048993.

84. Ashrafi, G., Wu, Z., Farrell, R.J., and Ryan, T.A. (2017). GLUT4 mobilization supports energetic demands of active synapses. Neuron *93*, 606–615.e3.

85. Janssen, R.J., van den Heuvel, L.P., and Smeitink, J.A. (2004). Genetic defects in the oxidative phosphorylation (OXPHOS) system. Expert Rev. Mol. Diagn. *4*, 143–156.

86. Rojas-Charry, L., Nardi, L., Methner, A., and Schmeisser, M.J. (2021). Abnormalities of synaptic mitochondria in autism spectrum disorder and related neurodevelopmental disorders. J. Mol. Med. (Berl) *99*, 161–178.

87. McGrath, T., Baskerville, R., Rogero, M., and Castell, L. (2022). Emerging evidence for the widespread role of glutamatergic dysfunction in neuropsychiatric diseases. Nutrients *14*, 917.

88. Oyarzábal, A., Musokhranova, U., Barros, L., and García-Cazorla, A. (2021). Energy metabolism in childhood neurodevelopmental disorders. EBiomedicine *69*, 103474.

89. Li, X., and Ascoli, G.A. (2008). Effects of synaptic synchrony on the neuronal input-output relationship. Neural Comput. *20*, 1717–1731.

90. Ikemoto, A., Bole, D.G., and Ueda, T. (2003). Glycolysis and glutamate accumulation into synaptic vesicles. Role of glyceraldehyde phosphate dehydrogenase and 3-phosphoglycerate kinase. J. Biol. Chem. *278*, 5929–5940.

91. Valenti, D., de Bari, L., De Filippis, B., Henrion-Caude, A., and Vacca, R.A. (2014). Mitochondrial dysfunction as a central actor in intellectual disability-related diseases: an overview of Down syndrome, autism, fragile X and Rett syndrome. Neurosci. Biobehav. Rev. *46*, 202–217.

92. Lin-Hendel, E.G., McManus, M.J., Wallace, D.C., Anderson, S.A., and Golden, J.A. (2016). Differential mitochondrial requirements for radially and non-radially migrating cortical neurons: implications for mitochondrial disorders. Cell Rep. *15*, 229–237.

93. Rossignol, D.A., and Frye, R.E. (2012). Mitochondrial dysfunction in autism spectrum disorders: a systematic review and meta-analysis. Mol. Psychiatry *17*, 290–314.

94. Slattery, C.F., Beck, J.A., Harper, L., Adamson, G., Abdi, Z., Uphill, J., Campbell, T., Druyeh, R., Mahoney, C.J., Rohrer, J.D., et al. (2014). R47H TREM2 variant increases risk of typical early-onset Alzheimer's disease but not of prion or frontotemporal dementia. Alzheimers. Dement. *10*, 602–608.e4.

95. Cserép, C., Schwarcz, A.D., Pósfai, B., László, Z.I., Kellermayer, A., Környei, Z., Kisfali, M., Nyerges, M., Lele, Z., Katona, I., et al. (2022). Microglial control of neuronal development via somatic purinergic junctions. Cell Rep. *40*, 111369.

96. Cserép, C., Pósfai, B., and Dénes, Á. (2021). Shaping neuronal fate: functional heterogeneity of direct microglia-neuron interactions. Neuron *109*, 222–240.

97. Boumezbeur, F., Mason, G.F., de Graaf, R.A., Behar, K.L., Cline, G.W., Shulman, G.I., Rothman, D.L., and Petersen, K.F. (2010). Altered brain mitochondrial metabolism in healthy aging as assessed by in vivo magnetic resonance spectroscopy. J. Cereb. Blood Flow Metab. *30*, 211–221.

98. Hickman, S.E., Kingery, N.D., Ohsumi, T.K., Borowsky, M.L., Wang, L.C., Means, T.K., and El Khoury, J. (2013). The microglial sensome revealed by direct RNA sequencing. Nat. Neurosci. *16*, 1896–1905.

99. Götzl, J.K., Brendel, M., Werner, G., Parhizkar, S., Sebastian Monasor, L., Kleinberger, G., Colombo, A.V., Deussing, M., Wagner, M., Winkelmann, J., et al. (2019). Opposite microglial activation stages upon loss of PGRN or TREM2 result in reduced cerebral glucose metabolism. EMBO Mol. Med. *11*, e9711.

100. Hyman, B.T., Van Hoesen, G.W., Damasio, A.R., and Barnes, C.L. (1984). Alzheimer's disease: cell-specific pathology isolates the hippocampal formation. Science *225*, 1168–1170.

101. Busche, M.A., Chen, X., Henning, H.A., Reichwald, J., Staufenbiel, M., Sakmann, B., and Konnerth, A. (2012). Critical role of soluble amyloid-β for early hippocampal hyperactivity in a mouse model of Alzheimer's disease. Proc. Natl. Acad. Sci. USA *109*, 8740–8745.

102. Šišková, Z., Justus, D., Kaneko, H., Friedrichs, D., Henneberg, N., Beutel, T., Pitsch, J., Schoch, S., Becker, A., von der Kammer, H., et al. (2014). Dendritic structural degeneration is functionally linked to cellular hyperexcitability in a mouse model of Alzheimer's disease. Neuron *84*, 1023–1033.

103. Kerchner, G.A., Hess, C.P., Hammond-Rosenbluth, K.E., Xu, D., Rabinovici, G.D., Kelley, D.A.C., Vigneron, D.B., Nelson, S.J., and Miller, B.L. (2010). Hippocampal CA1 apical neuropil atrophy in mild Alzheimer disease visualized with 7-T MRI. Neurology *75*, 1381–1387.

104. Montero-Crespo, M., Domínguez-Álvaro, M., Alonso-Nanclares, L., Defelipe, J., and Blazquez-Llorca, L. (2021). Three-dimensional analysis of synaptic organization in the hippocampal CA1 field in Alzheimer's disease. Brain *144*, 553–573.

105. Antonucci, F., Turola, E., Riganti, L., Caleo, M., Gabrielli, M., Perrotta, C., Novellino, L., Clementi, E., Giussani, P., Viani, P., et al. (2012). Microvesicles released from microglia stimulate synaptic activity via enhanced sphingolipid metabolism. EMBO J. *31*, 1231–1240.

106. Street, K., Risso, D., Fletcher, R.B., Das, D., Ngai, J., Yosef, N., Purdom, E., and Dudoit, S. (2018). Slingshot: cell lineage and pseudotime inference for single-cell transcriptomics. BMC Genomics *19*, 477.

107. Correale, C., Genua, M., Vetrano, S., Mazzini, E., Martinoli, C., Spinelli, A., Arena, V., Peyrin-Biroulet, L., Caprioli, F., Passini, N., et al. (2013). Bacterial sensor triggering receptor expressed on myeloid cells-2 regulates the mucosal inflammatory response. Gastroenterology *144*, 346–356.e3.

108. Mendonça, P.R.F., Tagliatti, E., Langley, H., Kotzadimitriou, D., Zamora-Chimal, C.G., Timofeeva, Y., and Volynski, K.E. (2022). Asynchronous glutamate release is enhanced in low release efficacy synapses and dispersed across the active zone. Nat. Commun. *13*, 3497.

109. Tagliatti, E., Bello, O.D., Mendonça, P.R.F., Kotzadimitriou, D., Nicholson, E., Coleman, J., Timofeeva, Y., Rothman, J.E., Krishnakumar, S.S., and Volynski, K.E. (2020). Synaptotagmin 1 oligomers clamp and regulate different modes of neurotransmitter release. Proc. Natl. Acad. Sci. USA *117*, 3819–3827.

110. Bennett, M.L., Bennett, F.C., Liddelow, S.A., Ajami, B., Zamanian, J.L., Fernhoff, N.B., Mulinyawe, S.B., Bohlen, C.J., Adil, A., Tucker, A., et al. (2016). New tools for studying microglia in the mouse and human CNS. Proc. Natl. Acad. Sci. USA *113*, E1738–E1746.

111. Qi, G., Mi, Y., and Yin, F. (2021). Characterizing brain metabolic function ex vivo with acute mouse slice punches. Star Protoc. *2*, 100559.

112. Wang, L., Chaudhari, K., Winters, A., Sun, Y., Liu, R., and Yang, S.H. (2022). Characterizing region-specific glucose metabolic profile of the rodent brain using Seahorse XFe96 analyzer. J. Cereb. Blood Flow Metab. *42*, 1259–1271.

113. Zheng, G.X.Y., Terry, J.M., Belgrader, P., Ryvkin, P., Bent, Z.W., Wilson, R., Ziraldo, S.B., Wheeler, T.D., McDermott, G.P., Zhu, J., et al. (2017). Massively parallel digital transcriptional profiling of single cells. Nat. Commun. *8*, 14049.

114. Hao, Y., Hao, S., Andersen-Nissen, E., Mauck, W.M., Zheng, S., Butler, A., Lee, M.J., Wilk, A.J., Darby, C., Zager, M., et al. (2021). Integrated analysis of multimodal single-cell data. Cell *184*, 3573–3587.e29.

115. Cahoy, J.D., Emery, B., Kaushal, A., Foo, L.C., Zamanian, J.L., Christopherson, K.S., Xing, Y., Lubischer, J.L., Krieg, P.A., Krupenko, S.A., et al. (2008). A transcriptome database for astrocytes, neurons, and oligodendrocytes: a new resource for understanding brain development and function. J. Neurosci. *28*, 264–278.

116. Cembrowski, M.S., Wang, L., Sugino, K., Shields, B.C., and Spruston, N. (2016). Hipposeq: a comprehensive RNA-seq database of gene expression in hippocampal principal neurons. eLife *5*, e14997.

117. Lein, E.S., Hawrylycz, M.J., Ao, N., Ayres, M., Bensinger, A., Bernard, A., Boe, A.F., Boguski, M.S., Brockway, K.S., Byrnes, E.J., et al. (2007). Genome-wide atlas of gene expression in the adult mouse brain. Nature *445*, 168–176.

118. Zimmerman, K.D., Espeland, M.A., and Langefeld, C.D. (2021). A practical solution to pseudoreplication bias in single-cell studies. Nat. Commun. *12*, 738.

119. Bankhead, P., Loughrey, M.B., Fernández, J.A., Dombrowski, Y., McArt, D.G., Dunne, P.D., McQuaid, S., Gray, R.T., Murray, L.J., Coleman, H.G., et al. (2017). QuPath: open source software for digital pathology image analysis. Sci. Rep. *7*, 16878.

120. Schafer, D.P., Lehrman, E.K., Heller, C.T., and Stevens, B. (2014). An engulfment assay: a protocol to assess interactions between CNS phagocytes and neurons. J. Vis. Exp. 51482.

STAR★METHODS

KEY RESOURCES TABLE

REAGENT or RESOURCE	SOURCE	IDENTIFIER
Antibodies		
Monoclonal mouse anti-Tom20	Santa-Cruz	Cat#sc-17764
Polyclonal rabbit anti-P2YR12	Anaspec	Cat#AS-55043A
Polyclonal guinea pig anti-IBA1	Synaptic Systems	Cat#234 308
Polyclonal rabbit anti-IBA1	WAKO Chemicals	Cat#019-19741
Polyclonal guinea pig anti-DCX	Merck-Millipore	Cat#AB2253
Polyclonal guinea pig anti-MAP2	Synaptic Systems	Cat#188 004
Polyclonal rabbit anti-vGlut1	Synaptic Systems	Cat#135 302
Monoclonal rat anti-CD68	Biolegend	Cat#137001
Polyclonal rabbit anti-Neurod2	Abcam	Cat#ab104430
Polyclonal rat anti-Ctip2	Abcam	Cat#ab18465
Monoclonal rat anti-CD45 Pe	Biolegend	Cat#103106
Monoclonal rat anti-CD45 PerCP	Biolegend	Cat#103130
Monoclonal rat anti-CD11b Pe-Cy7	Biolegend	Cat#101216
Monoclonal rat anti-CD16.32	Biolegend	Cat#101301
Monoclonal mouse anti-NeuN 488	Merck-Millipore	Cat#MAB377X
Anti-Puromycin 647	Scenith -Auguello Lab	RRID:AB_2827926
Polyclonal rabbit anti-PSD95	Thermo-Fisher	Cat#51-6900
Polyclonal rabbit anti-Trem2	R&D Systems	Cat#AF1729
Goat anti-Mouse IgG (H+L) Highly Cross-Adsorbed Secondary Antibody, Alexa Fluor 568	Thermo-Fisher	Cat#A11031
Goat anti-Rabbit IgG (H+L) Highly Cross-Adsorbed Secondary Antibody, Alexa Fluor 488	Thermo-Fisher	Cat#A11034
Goat anti-Rabbit IgG (H+L) Highly Cross-Adsorbed Secondary Antibody, Alexa Fluor 633	Thermo-Fisher	Cat#A21071
Goat anti-Rat IgG (H+L) Highly Cross-Adsorbed Secondary Antibody, Alexa Fluor 647	Thermo-Fisher	Cat#A21247
Goat anti-Guinea Pig IgG (H+L) Highly Cross-Adsorbed Secondary Antibody, Alexa Fluor 488	Thermo-Fisher	Cat#A11073
Goat anti-Guinea Pig IgG (H+L) Highly Cross-Adsorbed Secondary Antibody, Alexa Fluor 568	Thermo-Fisher	Cat.#A11075
Goat anti-Guinea Pig IgG (H+L) Highly Cross-Adsorbed Secondary Antibody, Alexa Fluor 633	Thermo-Fisher	Cat#A21105
Donkey anti-Sheep IgG (H+L) Highly Cross-Adsorbed Secondary Antibody, Alexa Fluor 488	Thermo-Fisher	Cat#A-11015
Donkey anti-Rabbit IgG (H+L) Highly Cross-Adsorbed Secondary Antibody, Alexa Fluor 568	Thermo Fisher	Cat#A-10042
Fluorsave	Millipore	Cat. #345789

(*Continued on next page*)

Continued

REAGENT or RESOURCE	SOURCE	IDENTIFIER
Chemicals, peptides, and recombinant proteins		
CNQX disodium salt	Tocris	Cat#1045/1
D-AP5	Tocris	Cat#0106/1
FCCP	Agilent Technologies	Cat#103015-100
Oligomycin	Agilent Technologies	Cat#103015-100
Rotenone/Antimycin A	Agilent Technologies	Cat#103015-100
Puromycin	Scenith/Auguello Lab	N/A
2-Deoxy Glucose	Scenith/Auguello Lab	N/A
Oligomycin	Scenith/Auguello Lab	N/A
Neuromag reagent	OZ-Biosciences	Cat#KC30800
Epoxy resin Poly/Bed® 812	Polysciences	Cat#08792-1
1% Uranyl Acetate	Electron Microscopy Sciences (EMS)	Cat#22400-1
4% Osmium Tetroxide	Electron Microscopy Sciences (EMS)	Cat#19140
Propylene Oxide	TAAB	Cat#P021
Hoechst-33342	Thermo-Fisher	Cat#62249
BioTracker ATP-Red Live Cell Dye	Merck-Millipore	Cat#SCT045
MitoTracker Deep Red FM	Thermo-Fisher	Cat#M22426
CellRosGreen reagent	Thermo Fisher	Cat#C1044
Anti-Mouse Ig, κ/Negative Control Compensation Particles Set	BD Biosciences	Cat#552843; RRID: AB_10051478
Anti-Rat Ig, κ/Negative Control Compensation Particles Set	BD Biosciences	Cat#552844; RRID: AB_10055784
Critical commercial assays		
Seahorse XF Cell Mito Stress Test Kit	Agilent Technologies	Cat#103015-100
Fixation/Permeabilization Solution Kit	BD Bioscience	Cat#554714
Foxp3 /Transcription Factor Staining Buffer Set	Thermo-Fisher	Cat#00-5523-00
Zombie NIR™ Fixable Viability Kit	Biolegend	Cat#423105
Chromium Next GEM Single Cell 3' Kit v3.1	10X Genomics	Cat# PN-1000269
Chromium Next GEM Chip G Single Cell Kit	10X Genomics	Cat# PN-1000127
Dual Index Kit TT Set A	10X Genomics	Cat# PN-1000215
Direct-Zol™ MiniPrep Isolation Kit	Zymo Research	Cat# R2050
High-Capacity cDNA RT kit	Applied Biosystems	Cat# 4368814
TaqMan Fast Universal PCR Master Mix(2x), no AmpErase UNG	Applied Biosystems	Cat# 4352042
Deposited data		
scRNA-seq data	This Paper	Geo number: GSE249036
Experimental models: Organisms/strains		
Mouse C56BL/6J	Charles River	Strain Code 632
Mouse: Trem2$^{-/-}$	Turnbull et al.[15]	N/A
Recombinant DNA		
pFU_GFP	Kirill Volynski, UCL	N/A
pAAV.hSynap.SF-iGluSnFR.A184V	Kirill Volynski, UCL	Cat#106175; RRID: Addgene_106175
Software and algorithms		
GraphPad Prism 9	GraphPad	https://www.graphpad.com; RRID:SCR_002798
Fiji	NIH	https://fiji.sc/; RRID:SCR_002285
Adobe Illustrator CC	Adobe	http://www.adobe.com/products/illustrator.html RRID:SCR_010279
Radius 2.0 software	EMSIS	https://www.emsis.eu/products/radius

(*Continued on next page*)

Continued

REAGENT or RESOURCE	SOURCE	IDENTIFIER
Seahorse Wave Version	Agilent Technologies	http://www.agilent.com/en-us/products/cell-analysis-(seahorse)/software-download-for-wave-desktop; RRID:SCR_014526
MetaFluor Fluorescence Ratio Imaging Software	Molecular Devices	RRID:SCR_014294
Matlab R2018 or R2021b	Mathworks	https://it.mathworks.com/; RRID: SCR_001622
FlowJo 10	FlowJo	https://www.flowjo.com/; RRID: SCR_008520
Bcl-convert 3.8.4	Bcl-convert	https://emea.support.illumina.com/sequencing/sequencing_software/bcl-convert.html
10x Genomics Cell Ranger 6.1.1	Cellranger	https://www.10xgenomics.com/; RRID:SCR_023221
R 4.2.2	R	https://www.r-project.org/; RRID: SCR_002394
Seurat 4.2.0	Seurat	https://satijalab.org/seurat/articles/get_started.html; RRID:SCR_016341
Bioconductor Milor 1.2.0	MiloR	https://www.bioconductor.org/packages/release/bioc/html/miloR.html
Slingshot 2.6.0	Slingshot	https://www.bioconductor.org/packages/release/bioc/html/slingshot.html[106]
pClamp-10	Axon Instruments, Foster City, CA	https://www.moleculardevices.com; RRID:SCR_011323
BrainWave 4	3Brain AG, Switzerland	https://www.3brain.com/products/software/brainwave4
Biorender	Biorender	http://biorender.com: RRID:SCR_018361
Viia7 software system	Applied Biosystems	http:https://www.thermofisher.com/it/en/home/life-science/pcr/real-time-pcr/real-time-pcr-instruments/viia-7-real-time-pcr-system.html RRID:SCR_023358
Imaris v. 9.7.2 or 7.2.3	Oxford Instruments	http://www.bitplane.com/imaris/imaris RRID:SCR_007370
QuPath v0.3.2	QuPath	https://doi.org/10.1038/s41598-017-17204-5

RESOURCE AVAILABILITY

Lead contact

Further information and requests for resources and reagents should be directed to and will be fulfilled by lead contact Michela Matteoli (michela.matteoli@hunimed.eu).

Materials availability

This study did not generate new unique reagents.

Data and Code availability

- Single-cell RNA-seq data have been deposited at GEO and are publicly available as of the date of publication. Accession numbers are listed in the key resources table.
- This paper does not report original code.
- Any additional information required to reanalyze the data reported in this paper is available from the lead contact upon request.

METHOD DETAILS

Mice

All experiments were performed in accordance with the guidelines established by the European Community Council (Directive 2010/63/EU of September 22nd,2010) and the Italian D.Lg. 26/2014. The study was approved by the Institutional Animal Care and Use Committee (IACUC) of the Humanitas Research Hospital and by the Italian Ministry of Health. C57BL/6J *Trem2*$^{-/-}$ mice, generated as previously described[15] were provided by Bioxell-Cosmo Pharmaceutical (Milan, Italy).[107] C57BL/6J mice were acquired by Charles River laboratories. Mice were housed in a Specific Pathogen Free (SPF) facility under constant temperature (22 ± 1C) and humidity (50%) conditions with a 12 hrs- light/dark cycle and were provided with food and water *ad libitum*. P0-1 and P18-20 male and female animals were used for each experiment, unless otherwise stated.

Primary hippocampal neuronal culture and transfection

Primary hippocampal neurons were isolated from either *Trem2*$^{+/+}$ or *Trem2*$^{-/-}$ P0-1 mice[15] and cultured in complete Neurobasal A medium (cat.10888, Thermo-Fisher) supplemented with 2% B27 (cat.17504044,Thermo Fisher Scientific). Briefly, hippocampi were dissected and dissociated by enzymatic digestion in 0.25% trypsin for 15 min at 37 °C and then triturated using a standard p1000 micropipette. Neurons were plated on poly-L-lysine (0.1 mg/mL; cat. P2636, Sigma-Aldrich)–coated 18-mm or 24-mm diameter glass coverslips at a density of 100,000 to 120,000 cells per coverslip (for imaging and electrophysiological experiments) or on poly-L-lysine (0.1 mg/mL) treated cartridges at a density of 12000 cells/well on XF-96 cell culture plates for Seahorse Extracellular Flux Analysis. Experiments were performed at 4-5 or 14-16 days *in vitro* (DIV). For both live imaging and immunofluorescence staining, hippocampal neurons were transfected at 5 DIV with either pFU_GFP or pAAV.hSynap.SF-iGluSnFR.A184V plasmid using Neuromag reagent (cat.KC30800; OZ Biosciences). This allowed expression of the iGluSnFR probe only in a small (∼3 to 5%) subpopulation of neurons, which was essential for imaging of vesicular release in individual synaptic boutons. The pFU_GFP and the pAAV.hSynap.SF-iGluSnFR.A184V plasmids were kindly provided by K. Volynski, University College London, London, UK.

Primary microglia culture

Primary microglia cultures were obtained from mixed glial cultures as previously described[43,44]). Briefly, meninges were removed from P2 newborn brains, then cortices and hippocampi were gently dissected in cold Hanks Balanced Salts Solution (HBSS, cat.14180046, Thermo Scientific). After digestion with trypsin at 37°C and mechanical dissociation, cells were plated in T-75 flasks and maintained in EMEM (cat.M5650, Sigma-Aldrich) containing 20% of heat-inactivated Fetal Bovine Serum (FBS, cat.ECS0186L, Euroclone), 0.6% glucose, 2mM sodium pyruvate (cat.ECM9542D, Euroclone) and 1% penicillin/streptomycin (cat.15140-122, Thermo Fisher). Microglia were isolated around DIV 15 by shaking flasks at 245 rpm speed for 60 minutes.

For conditioned medium preparation, microglial cells were plated on poly-L Ornithine (cat. P8638, Sigma Aldrich) pre-coated 6-multiwell in Neurobasal-A/B27 medium at a density of 1x106 cells/well. After 24 hours *in vitro*, Conditioned Medium (CM) was collected and centrifuged 1000 x g for 20 minutes, then used for subsequent experiments.

Live-imaging experiments

ATP imaging in 4DIV neuronal cultures

4DIV primary hippocampal neurons obtained from *Trem2*$^{+/+}$ and *Trem2*$^{-/-}$ newborn pups were loaded with the mitochondrial ATP biotracker ATP-red live cell dye (cat.SCT045, Merk-Millipore) for 45 min at 37 C in Neurobasal-A Medium and then imaged for measuring mitochondrial ATP production. Somatic neurons were identified by either sparse GFP transfection or by bright-light images of neuronal soma. Neurons were maintained in the extracellular buffer 1. The extracellular buffer (EB1) contained 125 mM NaCl, 2.5 mM KCl, 2 mM MgCl2, 2 mM CaCl2, 30 mM glucose, and 25 mM Hepes (pH 7.4).[108,109] After 2 mins recording of basal ATP-red fluorescence, mitochondrial complex 1 blocker Rotenone plus Antimycin A (0.5 μM, cat.103015-100, Agilent Technologies) was applied to the cells and ATP decay measured for an additional 10 minutes. Time-lapse recording of ATP dynamics was performed with an acquisition rate of 0.2 Hz. A 18-mm recording chamber (cat.QR-40LP, Warner Instruments, Hamden, CT) was placed on the stage of an IX-71 inverted microscope (Olympus, Hamburg, Germany) equipped with an EMCCD (electron-multiplying CCD) camera (QuantEM-SC 512x512, Photometrics). Illumination was obtained using a light-emitting diode LED (Cairn research, Optoled Lite), coupled to the acquisition software (MetaFluor, Molecular Devices) to minimize photobleaching. A 40X (1,3 numerical aperture; N.A.) oil-immersion objective was used to identify multiple neuronal somas in the field of view (∼256 x 256 pixel). ATP decays were measured as ΔF/F0. $\Delta F_{rotenone}$ was then measured to determine mitochondrial ATP production. All values were normalized to *Trem2*$^{+/+}$ neurons.

Dual-color synaptic imaging in 14DIV neuronal cultures

14-16 DIV hippocampal neurons obtained from *Trem2*$^{+/+}$ and *Trem2*$^{-/-}$ newborn pups and transfected with iGluSNFR probe were incubated for 45 mins at 37°C with the mitochondrial ATP biotracker ATP-red live cell in Neurobasal-A medium. Neurons were first stimulated with 5 stimuli at 10 Hz and recorded in the green channel to measure glutamate release at individual boutons. After 5 minutes of recovery, synaptic ATP-red signal was recorded in the red channel on the very same boutons. To evoke mitochondrial ATP production in synapses, neurons were challenged with 200 stimuli at 100 Hz and ATP dynamics recorded for 10 mins. Dual color imaging experiments were conducted in an open laminar flow field-stimulation chamber (cat.QR/RC-47FSLP, Warner Instruments, Hamden, CT) at 23 to 25°C. The extracellular buffer (EB1) contained 125 mM NaCl, 2.5 mM KCl, 2 mM MgCl2, 2 mM CaCl2, 30 mM

glucose, and 25 mM Hepes (pH 7.4)[108,109]. To block recurrent activity, EB1 was supplemented with 6-Cyano-7-nitroquinoxaline-2,3-dione (CNQX) (25 μM; cat.479347-85-8, Tocris) and DL-AP5 (50 μM; cat.79055-68-8, Tocris). Electrical-evoked responses were induced by delivering 1 msec pulses with an amplitude 100 m using a train generation unit (Digitimer Ltd, DG2A) connected to a stimulus isolation unit (SIU-102; Warner Instruments, Hamden, CT). Recording chambers were placed on the stage of an IX-71 inverted microscope (Olympus, Hamburg, Germany) equipped with an EMCCD (electron-multiplying CCD) camera (QuantEM-SC 512x512, Photometrics). Illumination was obtained using a light-emitting diode LED (Cairn research, Optoled Lite), coupled to the acquisition software (MetaFluor, Molecular Devices) to minimize photobleaching. A 40X (1.3 numerical aperture; N.A.) oil-immersion objective was used to identify an axonal branch of an iGluSNFR positive neuron. Evoked iGluSNfr or ATP-red responses were recorded in an ~240x60 μm (898x224 pixels) region of interest (ROI) typically containing 20 to 100 individual boutons. Time-lapse recording of glutamate dynamics was performed with an acquisition rate of 67 Hz for ~8 seconds, while recording of mitochondrial ATP was performed with an acquisition rate of 0.2 Hz for 12 minutes. Images were analyzed using ImageJ (NIH) and MATLAB (MathWorks) custom-made software scripts.[109] Glutamate synaptic responses were identified by subtracting the resting iGluSNFR fluorescence from the peak fluorescence after a 10-Hz burst of 5 APs. This was followed by the generation of ~1 μm ROIs that were used to measure the average fluorescence response in all identified boutons in each experiment. After subtracting the background, the data were normalized to the resting iGluSNFR or ATP-red signal (ΔF/F0).

Seahorse Extracellular Flux Analysis in primary cultures

The bioenergetic properties of primary hippocampal neurons and cultured microglia obtained from Trem2$^{+/+}$ and *Trem2*$^{-/-}$ newborn pups were determined using the XF-96 Seahorse extracellular flux analyzer (Seahorse Bioscience, CA). Neurons and microglia were grown at 37°C, with 5% CO_2, up to 4 DIV (neurons) or for 24 hours (microglia). At indicated time points, neurons and microglia were washed and assayed in the XF Assay medium, XF DMEM pH 7.4 supplemented with 10 mM glucose, 1 mM pyruvate sodium and 2 mM L-Glutamine (cat.103575,103578,103577 and 103579, Agilent Technologies) for Mito Stress Test respiration measurements according to the manufacturer's protocol. Measurements were obtained in real-time with no drug treatment (basal conditions) and with the sequential injection of 1.5 μM Oligomycin, 1.5 μM FCCP, 0.5 μM Rotenone plus Antimycin A (Rot/AA) (cat.103015-100, Agilent Technologies). Oxygen Consumption Rate (OCR) data were obtained as picomoles of O_2 consumption in the media and normalized against the control condition. OCR measurements under basal conditions in the absence of drugs represent the basal OCR. OCR measurements after FCCP injection represent the maximal OCR. OCR measurements after Oligomycin injection represent the ATP-coupled respiration. OCR measurements after Rot/AA injection represent the non-mitochondrial residual respiration. Three cycles of measurements were acquired for each condition. At least 15 replicates for each condition, for each experiment, have been assayed. OCR values, under basal condition and after the drugs' additions were then plotted and run for statistical analysis using GraphPad Prism.

Ex vivo *FACS measurements*

P1 hippocampi were carefully dissected in cold HBSS under a stereotactic microscope and mechanically digested in ice with cold buffers at 4°C as previously.[110]

Cells were first incubated with FC blocking CD16.32 (cat.101301, clone 93, 1:100, Biolegend) for 15', then incubated in FACS buffer (2% FBS, 1 mM EDTA in phosphate buffer saline) with the following fluorescently conjugated antibodies: CD45-Pe or PerCP (cat.103106 and 103130, clone 30-F11; 1:500, Biolegend), CD11b-Pe-Cy7 (cat.101216, clone M1-70; 1:200, Biolegend) for 30' in ice. After surface staining, samples were washed twice with FACS buffer and centrifuged at 300xg for 5' at 4°C. Viability dye staining was then performed for 15' by resuspending the samples in phosphate buffer saline (PBS, cat.TL1006, Microgem) containing Zombie Nir (cat.423105, 1:800, Biolegend). For intracellular staining FOXP3 buffer kit (cat.00-5523-00, Thermo-Fisher) was used. Permeabilization and fixation, as well as subsequent washing steps incubations and centrifugations, were performed according to the protocol. Intracellular staining was performed for 1h on ice and the following antibodies were used: anti-NeuN 488 (cat.MAB377X, clone A60; 1:300 Merck-Millipore), anti-Puromycin AF647 (cat.AB_2827926, clone R4743L-E8; 1:400, Auguello Lab). For metabolic staining, the cells were incubated with CellROXgreen (cat.C1044, Thermo-Fisher) or with Mitotracker Deep Red FM (cat.M22426, Thermo-Fisher) for 35' at 37°C. Metabolic staining was not ''coupled'' with intracellular staining. FACS analysis was performed on a FACS Fortessa machine or FACS Canto II (BD Biosciences), and data were analyzed with FlowJo Software (TreeStar).

Single Cell ENergetIc metabolism by profilIng Translation inHibition Assay

SCENITH™ was performed according to Argüello et al.,[49] with minor modifications (www.scenith.com). After dissection, hippocampi were digested following a papain-based protocol (cat.LK003153, Worthington Biomedical) for 45' minutes at 37°C under continuous agitation. After neutralizing the reaction with Neurobasal-A medium supplemented with 10% FBS, digested hippocampi were gently homogenized with a P1000 pipette, filtered with a 70μm strainer, and centrifuged at 300xg for 10' at RT. The obtained cell suspension was then resuspended and plated at a density of 150.000 cell/well in a 96 multi-well plate. Cells were allowed for an additional 45' for recovery at 37°C and 5% CO_2, after which they were incubated with a mix of different metabolic inhibitors for 10' at 37°C and 5% CO_2. The following metabolic inhibitors were used: 100 μM 2-Deoxy Glucose, 1μM Oligomycin, 2-Deoxy Glucose combined with Oligomycin (same concentrations as stated above, Scenith). Next, 10μg/ml Puromycin was applied to the samples, and left in incubation for 45' at 37°C and 5% CO_2. Cells were then washed twice in FACS buffer and centrifuged at 300xg 4°C for 5' and processed for FACS as described in the previous paragraph.

Seahorse Extracellular Flux Analysis in hippocampal slices

The bioenergetic properties of *ex vivo* acute brain slices obtained from *Trem2*$^{+/+}$ and *Trem2*$^{-/-}$ male offspring aged P1 or P18, were determined using the XF-96 Seahorse extracellular flux analyzer (Seahorse Bioscience, CA) with adapted protocol.[111,112] Mice were

deeply anesthetized by CO_2 inhalation and then decapitated. Brains were rapidly removed and immediately immersed in ice-cold dissection aCSF solution previously saturated for at least 15 minutes with 95% O_2 and 5% CO_2. aCSF solution contained (in mM): 129 NaCl, 1.25 NaH_2PO_4, 10 glucose, 1.8 $MgSO_4$, 1.6 $CaCl_2$, 3 KCl, 21 $NaHCO_3$. Coronal hippocampus slices (300 μm) were cut using a VT1000S vibratome (Leica Biosystems Nussloch GmbH) and maintained at 4°C in a high-sucrose protective solution at 35 °C for a minimum of 60 minutes before being used for the forthcoming processing.

For tissue subprocessing, 1mm-diameter 300 μm-thick punches covering hippocampal CA area on P1, and both CA1 and CA3 subfield areas for P18 brain slices were manually obtained with a 1-mm Rapid-Core sampling puncher (Ted Pella, Inc). Punches were rapidly immersed in oxygenated Assay medium (in mM, 130 NaCl, 5 KCl, 1.2 KH_2PO_4, 1.2 $MgSO_4$, 2 $CaCl_2$, 25 HEPES, 0,01 Pyruvate and 6 Glucose, pH 7.4) and plated into a XF-96 cell culture plate, single punch/well, previously coated with poly-D-Lysine (0.1 mg/ml). Punches were washed and assayed in the XF Assay medium for Mito Stress Test respiration measurements. Measurements were obtained in real-time with no drug treatment (basal conditions) and with the sequential injection of 2.5 μM Oligomycin, 1.5 μM FCCP, 0.5 μM Rotenone plus Antimycin A (Rot/AA) (cat.103015-100, Agilent Technologies). Oxygen Consumption Rate (OCR) data were obtained as picomoles of O_2 consumption in the media and normalized against the control condition within each experiment. Given the slower kinetics in sliced tissues, 8 cycles of measurement were used for most conditions. OCR measurements under basal conditions in the absence of drugs represent the basal OCR. OCR measurements after FCCP injection represent the maximal OCR. OCR measurements after Oligomycin injection represent the ATP-coupled respiration. OCR measurements after Rot/AA injection represent the non-mitochondrial residual O_2 consumption. OCR values, under basal condition and after the drugs' additions, were normalized within each experiment over the *Trem2*$^{+/+}$ counterpart, then plotted and run for statistical analysis using GraphPad Prism. Samples that did not display basal respiration values above the advisable ranges (>10 pmol/min) or did not respond to Seahorse drugs were discarded from the analysis.

RNAseq analysis

Sample preparation

P1 hippocampi from *Trem2*$^{+/+}$ and *Trem2*$^{-/-}$ pups from 3 independent litters (n = 2 embryos per sample per litter) were rapidly dissected in ice cold HBSS solution and pooled together. A balanced pool of males and females in both control and Trem2$^{-/-}$ mice were employed, to minimize the sex effect.

Dissected tissue was dissociated using Papain Dissociation System kit (Worthington, cat#LK003150) following the manufactured instructions as previously optimized. Dissociated hippocampi were suspended in PBS supplemented with 0.02% BSA (Sigma Aldrich). Around 8,000 cells per sample were loaded into one channel of the Single Cell Chip G using the Single Cell 3′ v2.1 single cell reagent kit (10X Genomics) for Gel Bead Emulsion generation into the Chromium system. Following capture and lysis, cDNA was synthesized and amplified for 14 cycles following the manufacturer's protocol (10X Genomics). 50 ng of the amplified cDNA were then used for each sample to construct Illumina sequencing libraries. Sequencing was performed on the NextSeq2000 Illumina sequencing platform following 10x Genomics instruction for reads generation.

Single cell sequencing analysis

Raw sequencing data were converted to fastq files using Illumina bcl-convert tool, integrated into the CellRanger (10X Genomics) suite (version 6.1.1.[113] The CellRanger analysis pipeline was used to generate a digital gene expression matrix starting from raw data. Pre-build mouse genome (version mm10-1.2.0) was used as genome reference. CellRanger count module was used to map reads with default settings setting and sequence length set to r1-length = 28 and–r2-length = 90. At least 35,000 reads per cell were produced for each sample. The raw digital gene expression matrix (UMI counts per gene per cell) was imported in R version 4.4.2 using Seurat R package 4.2.0[114] Briefly, UMI counts per gene per cell for each biological replicate was imported in Seurat and sample quality control was assessed by filtering out cells meeting any of the following criteria: less than 1,000 unique genes expressed, less than 1,000 UMIs, or more than 10.0% of reads mapping to mitochondria. For each time point, data were normalized for cell feature expression by multiplying its total expression by a scale factor of 10,000, and log+1-transformation of the result. This was followed by assignment of cell cycle scores to individual cells based on the expression of G2/M and S phase markers. We next scaled the expression values and identified the 2,000 most variable genes with FindVariableFeatures Seurat function (selection.method = ''vst'', nfeatures = 2000). We then performed principal component analysis (PCA) linear dimensionality reduction on the scaled data and clustered the cells with a graph-based clustering approach (RunPCA). We perform SCT-Normalization (negative binomial regression) without regressing out any variable (SCTransform(seurat, vars.to.regress = NULL, return.only.var.genes = T) for each individual sample. Due to differences in cell clustering due to the sex, we integrated the data using Seurat built-in SelectIntegrationFeatures(nFeatures = 3,000), followed by PrepSCTIntegration, FindIntegrationAnchors(normalization.method = "SCT") and IntegrateData functions. To choose the number of principal components we used a graph-based method (elbow plot). We then clustered the cells using the Louvain algorithm (within Seurat) to iteratively group cells together. Optimal resolution was chosen by analyzing the cluster tree plot (clustree). To annotate clusters, we determined differentially expressed genes using FindAllMarkers function embedded in Seurat (Wilcoxon Rank Sum test with Bonferroni correction for multiple testing; adjusted $P < 0.05$). We tested only genes that were detected in a minimum of 40% of the cells within the cluster and that showed, on average, at least a 0.25-fold difference (log-scale) between the cells in the cluster and all remaining ones. By reviewing the resulting markers, as well as the expression of canonical marker genes and additional markers from the literature,[115–117] we assigned a cell-type identity. We then filtered out vascular, mesenchymal and ependymal cells and re-clustered the remaining cells as previously described.

To test the differential cells abundances between genotypes, we used MiloR 1.2.0 function on the KNN-graph generated from the latent space embeddings with default parameters, where 'genotype' was used as a covariate.

Cell type-specific differential gene expression analysis

To determine differentially expressed genes, we used FindMarkers from Seurat function implemented with default two-part hurdle model (MAST) with added random effect variables (MAST-re test; adjusted $P < 0.05$)[118] testing only genes found in at least 20% of cells within the cluster and that showed, on average, at least a 0.10-fold difference (log-scale) across genotypes and setting the batch as random effect variable. The list of differentially expressed genes of CA-ImmPyr, CA1-Pyr and CA3-Pyr cell types was analyzed using the Ingenuity Pathway Analysis (IPA - Qiagen Ingenuity Systems) canonical pathways enrichment.

Trajectory analysis

Pseudotime and trajectory tree were inferred using the Slingshot package in a two-step process. First, we identified the global lineage structure with a cluster-based minimum spanning tree (MST). Then, we fit simultaneous principal curves to describe each lineage onto the UMAP space using the slingshot function. Trajectory inference and visualization were performed on integrated pre-processed data object UMAP space and with previously assigned cell type labels. Apical Progenitor cells (AP) were chosen as the root of the trajectory. All the inferred pseudotime variables (one per lineage) are added to the metadata, individually. We next compared pseudotime distribution of cells in the three lineages by randomly subsetting 100 cells per each lineage and performing a two-sided Kolmogorov-Smirnov test of the empirical cumulative distribution functions. Finally, we repeated the same procedure to compare pseudotime distribution of cells for each genotype for individual cell types for each lineage.

RNA extraction and qRT-PCR

Either frozen hippocampi from P1, P20, P90 or CA1/CA3 1-mm punches from *Trem2*$^{+/+}$ P18 mice were gently thawed on ice and then subjected to mechanical disruption with homogenizing beads onto automatic Tissue Lyser, in 500 μl TRI Reagent® (Zymo Research). RNA was isolated with RNA Direct-Zol™ MiniPrep Isolation Kit (Zymo Research), according to the manufacturer guidelines. RNA was eventually eluted in 25 μl DNAse/RNAse-free water and quantified with NANOdrop 2000c spectrophotometer (Thermo Fisher Scientific) for RNA concentration and 260/280 nm optical density ratios.

500 ng RNA for each condition underwent reverse transcription into cDNA with High-Capacity cDNA RT kit (Applied Biosystems). Quantitative Real-time polymerase chain reaction (qRT-PCR) was performed with TaqMan detection kit (TaqMan Fast Universal PCR Master Mix(2x), no AmpErase UNG, ThermoFisher) onto qRT-PCR Viia7 software system (Applied Biosystems) in a final volume of 10 μl. Each gene was subjected to at least duplicate measurements and data analyses were performed with the comparative ΔC_T method. mRNA measurements for each target gene were normalized to the housekeeping gene *Gapdh*. The following TaqMan assays were used (Applied Biosystems): mouse *Trem2* FAM-MGB Mm04209424_g1; mouse GAPD(GAPDH) VIC-MGB Endogenous Control.

Electrophysiology

Primary neuronal cultures

Whole cell voltage-clamp recordings were performed on 4DIV primary hippocampal neurons from *Trem2*$^{+/+}$ and *Trem2*$^{-/-}$ P1 mice. During recordings, neurons were mantained in extracellular buffer 2 in an 18-mm recording chamber (cat.QR-40LP, Warner Instruments, Hamden, CT). The extracellular buffer (EB2) contained (in mM): 125 NaCl, 5 KCl, 1.2 $MgSO_4$, 1.2 KH_2PO_4, 2 $CaCl_2$, 6 glucose, and 25 HEPES-NaOH, pH 7.4. Recording pipettes (resistances of 3-5 MΩ) were filled with a standard intracellular solution containing (in mM): 135 K^+-gluconate, 1 EGTA, 10 HEPES, 2 $MgCl_2$,4 MgATP, and 0.3 Tris-GTP, (pH 7.4). For voltage-dependent current activation experiments, neurons were held at −70 mV and incremental depolarizing steps (10mV for 500ms), starting from -120 and heading to +70 mV, were applied. Na^+ current density was obtained by dividing peak inward current by cell capacitance (nA/pF). Resting potential was calculated at I = 0 in current clamp configuration, whereas input resistance was calculated in voltage clamp configuration by using I/V relationship slope of the steady state current measured at different depolarizing voltage steps (from −100 to -70 mV). Recordings were performed in voltage clamp mode using a Multiclamp 700B amplifier and pClamp-10 software (Axon Instruments, Foster City, CA). Series resistance ranged from 10 to 20 MΩ and was monitored all over the whole recordings. Signals were amplified, sampled at 10 kHz, filtered to 2 or 3 KHz, and analyzed using the pClamp 10 data acquisition and analysis program. Cells in culture with leak currents >100 pA were excluded from the analysis.

Multi-Electrode-Arrays (MEA) on brain slices

P18 *Trem2*$^{+/+}$ and *Trem2*$^{-/-}$ male mice were deeply anesthetized by CO_2 inhalation and then decapitated. Brains were dissected out and immediately immersed in ice-cold dissection aCSF solution previously saturated for at least 15 minutes with 95% O2 and 5% CO2. aCSF solution contained (in mM): 129 NaCl, 1.25 NaH_2PO_4, 10 glucose, 1.8 $MgSO_4$, 1.6 $CaCl_2$, 3 KCl, 21 $NaHCO_3$. Coronal hippocampus slices (400 μm) were cut using a VT1000S vibratome (Leica Biosystems Nussloch GmbH) and maintained at 4°C in a high-sucrose protective solution at 35°C for a minimum of 60 minutes before being used for recordings. During the recordings, slices were placed on the multielectrode array and perfused with aCSF at 2 ml/min speed. After 15 minutes of slice spiking activity stabilization, spontaneous extracellular signals were collected for additional 5-10 minutes.

All extracellular multisite recordings were performed using a CMOS biosensor and acquisition system (3Brain AG, Switzerland). High-Density Multielectrode CMOS Arena chips integrating 4096 recording electrodes in a 64 x 64 array configuration were employed. The acquisition was controlled by software BrainWave 4 (3Brain AG, Switzerland). Raw data were digitized at 18kHz.

For each experiment an image of the slice in the recording unit was acquired. Only the electrodes located in the CA1 and CA3 regions were analyzed. Custom-written MATLAB scripts were used for all MEAs analysis algorithms. At first, noise signals were

identified and excluded from the analysis. Recordings were then high-pass filtered (350 Hz) using a second-order Butterworth filter with BrainWave Software (3Brain Gmbh, Switzerland). A spike detection algorithm (Precise Timing Spike Detection, PTSD) was implemented to extract spike times from the 18 kHz signal. A threshold of 7 standard deviations (SDs) was set to filter out basal noise.

Spikes that occurred within the refractory period (set to 1 ms) were removed. Timestamps of every detected neuron were used to create raster plots. The average firing rate per neuron was calculated by dividing the total number of spikes by the recording session duration. To assess the interaction between the hippocampal subregions, a suitable cross-correlation measure was calculated using MATLAB xcorr function. To determine the degree of synchronization between different neuronal firing patterns, the maximum correlation at zero lag was calculated and a correlation matrix was built for each experiment and the mean correlation coefficient estimated for each experiment. The number of neurons analyzed, instead, corresponded to the number of active electrodes sampled for each hippocampal subregion.

Immunofluorescence analysis

Hippocampal slices

P1 pups were sacrificed by decapitation and the brains quickly removed from the skull, washed in fresh PBS1X and fixed in 4% paraformaldehyde (PFA) overnight. P18 were deeply anesthetized with xylazine/ketamine mixture and transcardially perfused with 4% PFA and additionally post-fixed overnight. Coronal slices (50μm thick) were cut with a VT1000S vibratome (Leica Microsystems). Slices were washed in cold PBS1X, and permeabilized with 0.2% Digitonin in PBS1X for 15 mins or 0.5% TritonX-100 in PBS1X for 1 hour and nonspecific binding sites were blocked by incubation for 30 min with either 5% normal goat serum (NGS), 2% Bovine Serum Albumin (BSA) or donkey serum (DS) and 0.5% TritonX-100 in PBS1X before an overnight incubation at 4C with primary antibodies.

Slices were then washed 3 times with PBS and incubated with secondary antibodies conjugated to Alexa Fluor (488, 555, or 633). The following primary antibodies were used: guinea pig anti-IBA1 (cat.234 308, 1:1000, Synaptic Systems), rabbit anti-IBA1 (cat.019-19741, 1:1000, WAKO Chemicals), rabbit anti-P2yr12 (cat.AS-55043A, 1:400, Anaspec), mouse anti-Tom20 (cat.sc-17764, 1:200, Santa Cruz), guinea pig anti-DCX (cat.AB2253, 1:500, Merck-Millipore), guinea pig anti-MAP2 (cat.188 004, 1:1000, Synaptic System), rat anti-CD68 (cat.137001, 1:1000, Biolegend), rabbit anti-PSD95 (cat.51-6900, 1:200, Thermo-Fisher), sheep anti-Trem2 (cat.AF1729, 1:200, R&D Systems), rabbit anti-Neurod2 (cat.ab104430, 1:1000, Abcam), rat anti-Ctip2 (cat.ab18465, 1:100, Abcam). All slices were counterstained with Hoechst-33342 (cat.62249, 1:1000, Thermo-Fisher) and mounted with Fluorsave (cat.345759, Millipore). Images were acquired using a Leica SP8I or a SP8II laser scanning confocal microscope equipped with an HC PL APO 20x/0.75 CS2 objective and ACS APO 40x or 63x/1.40 oil immersion objective. For Tom20 analysis, the entire pyramidal layer (P1) or a region of CA1 and CA3 hippocampal subfield (P18) were acquired using 40x or 60x oil immersion objective. Tom20 fluorescence intensity was estimated by generating a binary mask created on Dcx or Map2 staining of CA1 and CA3 pyramidal layer and normalized by area fraction. For staining related to Figure 5, a subset of control animals from Figures 3 and 4 was used. Neuronal density was estimated by counting NeuroD2-positive cells in the CA1 and CA3 pyramidal layer areas using Positive Cell Detection function implemented in QuPath software.[119] Similarly, microglia density was estimated by counting Iba1 positive cells and normalized per CA1 and CA3 area. Hippocampal microglia morphology was assessed using Skeleton plugin in Fiji software (NIH, Bethesda), which enables a three-dimensional (3D) morphological analysis of skeletonized microglia present in tissue. P2y12r intensity at single hippocampal microglia cells was measured by generating a binary mask created on 3D Iba1 labeling. Microglia phagocytosis and Trem2 immunoreactivity were assessed by performing three-dimensional surface rendering and volumetric quantification using Imaris Software (Oxford Instruments, v. 9.7.2,).[120] PSD95 intensity was measured as volume fraction of the whole image. For quantification of PSD95 engulfment, only the signal co-localized with CD68 within microglia was considered.

Primary hippocampal neurons

4DIV or 14DIV neurons were fixed with 4% PFA in PBS1X and sucrose solution for 20 min and permeabilized with 0.1% Saponin in PBS1X for 10 min. Nonspecific binding sites were blocked by incubation for 30 min with 5% NGS and 0.1% Saponin in PBS1X before a 2-h incubation at room temperature with primary antibodies. Neurons were washed 3 times with PBS1X and incubated with secondary antibodies conjugated to Alexa Fluor (488, 568, or 633) for 45 min at room temperature. Coverslips were washed 3 times in PBS1X, counterstained with Hoechst to reveal nuclei and mounted onto slides with Fluorsave. The following primary antibodies were used: mouse anti-Tom20 (cat.sc-17764; 1:200, Santa Cruz); guinea pig anti-Map2 (cat.188004; 1:1000, Synaptic Systems) and rabbit anti-VGlut1 (cat.135302; 1:1000, Synaptic Systems). Somatic and neuritic or synaptic fluorescence intensity was quantified using ImageJ (NIH). Somatic and neuritic Tom20 fluorescence intensity, corrected for background signal, was estimated by manual tracking of cell bodies and primary neurites while Tom20 synaptic intensity was quantified by generating a binary mask created from the vGlut1 staining over-imposing GFP positive neurons.

Sholl analysis of 4DIV sparsely distributed neurons was performed using the Sholl analysis Fiji plugin. Briefly, circles of increasing radius, originating from the center of the transfected cell body, were drawn, and the numbers of intersections between dendritic branches and the edges of the circles were used as an estimate of neuronal arborization. Images were acquired using a Leica SP8I confocal microscope equipped with an ACS APO 40x or 63x oil immersion objective.

Electron microscopy

P18 slices

Trem2$^{+/+}$ and *Trem2*$^{-/-}$ male mice at P18 deeply anesthetized with xylazine/ketamine mixture and transcardially perfused with fresh PBS1X. Brains were removed and placed in ice-cold solution containing the following (in mM): 129 NaCl, 1.25 NaH_2PO_4, 10 glucose,

1.8 $MgSO_4$, 1.6 $CaCl_2$, 3 KCl, 21 $NaHCO_3$ (pH 7.4), equilibrated with 95% O_2 and 5% CO_2. Coronal slices (300 mm thick) were cut with a VT1000S vibratome (Leica Microsystems) from medial Prefrontal Cortex (PFC). Slices were washed in cold PBS1X and then fixed for 3 hours with 2.5% glutaraldehyde in 0.1M Na^+Cacodylate buffer at room temperature. Slices were post-fixed in 4% osmium tetroxide (cat.19140, Electron Microscopy Science, Hatfield, PA, USA) for 2 hours and in 1% aqueous uranyl acetate (cat.22400-1, Electron Microscopy Science) for 1 hour at room temperature.

Slices were then dehydrated through a graded ethanol series with propylene oxide as a transition fluid (cat.P021, TAAB Laboratories Equipment, Aldermaston, UK) and embedded in epoxy resin (Poly-Bed; cat.08792-1, Polysciences, Warrington, PA, USA) overnight at 42°C e ultimately for 2 days at 60°C. Subsequent examination of the regions of interest (hippocampal CA1 and CA3 regions) was performed on 200 nm semithin sections stained with Toluidine Blue. Ultrathin sections (50 nm) were then cut and counterstained with 1% uranyl acetate. Electron micrographs were acquired using a HT7800 120 kV transmission electron microscope equipped with Megaview III digital camera and Radius 2.0 software (EMSIS, Muenster, Germany). Tile scan images were acquired to quantify the major axis length of mitochondria in pyramidal neurons somata. Single electron micrographs were used to acquire synapses in the pyramidal layer of both CA1 and CA3 regions. Morphometric analysis was done using Fiji software (NIH, Bethesda). Postsynaptic electron density was used to identify excitatory synapses. Structures with sagittal diameter between 20 and 80 nm were classified as SVs. SVs touching AZ were classified as docked SVs.

Statistical analysis

The distribution of data in each set of experiments was first tested for normality using the Shapiro–Wilk test. The similarity of variances between each group of data was tested using the F test. Normally distributed data are presented as mean ± SEM; each plot also contains the individual data points. Unpaired Student's *t* tests for group means, One-Way ANOVA or Two-Way ANOVA followed by post-Hoc multiple comparisons test was used as indicated. To compare datasets that failed the normality test, Mann–Whitney U test and ANOVA on Ranks followed by Dunn's multiple comparison test were used as indicated. No statistical methods were used to predetermine sample sizes, but our sample sizes are like those reported in previous publications in the field. All statistical tests were performed using GraphPad9 (Prism software).